A non-classical computational method for modelling functionally graded porous planar media using micropolar theory

Abstract

The current study proposes a computational-based method to employ the non-classical micropolar continuum for modelling plates with in-plane functionally graded porosities. Initially, a homogenisation method is developed to derive the micropolar parameters of porous heterogenous plates based on strain energy equivalence in various designed deformations simulated via finite element analysis. The modelling procedure is further augmented to accommodate structures with functionally graded porosities. The established method offers an effective framework for studying the mechanical behaviour of porous plates with various porosity distributions and a wide range of aspect ratios. Results indicate that the micropolar theory-based modelling surpasses traditional Cauchy theory in accurately predicting the stiffness and displacement distribution of the FG porous structures. The novelty of this study lies in the integration of micropolar theory with the homogenisation of graded porosity patterns, offering enhanced predictions for materials with microstructural features. Additionally, a custom finite element formulation is developed in COMSOL to implement micropolar elasticity, significantly improving the computational efficiency to account for complex geometry, loading, and boundary conditions. To show the applicability of the method, the modelling is used to design a dental implant with its functional property mimicking that of the natural bone to avoid stress-shielding while ensuring proper occlusivity.

Keywords: Modelling Functionally Graded Porosity; Micropolar and Cauchy continua; Finite Element Analysis; Equivalent Porous-Cellular Materials; Homogenisation.

1 Introduction

The customisable properties [1], high specific surface area, and lightweight nature of porous materials have made them key elements in various engineering applications. In recent decades, porous materials have been widely used in many industrial sectors, including aerospace, civil engineering, and biomedical applications such as porous implants and meshes for guided bone regeneration [2], [3], [4]. Particularly, functionally graded porous structures [5], characterised by a graded distribution of porosity, can provide customised mechanical properties along spatial gradients [6], [7]. The mechanical behaviours of porous FG structures are of interest in the current literature in terms of static, vibration, and buckling problems, specifically in beams, plates, and shells [8], [9], [10], [11], [12].

The thermo-mechanical behaviour of two-directional functionally graded porous-auxetic metamaterial has been the topic of a study by Behravanrad and Jafari [10], where, through a numerical finite difference scheme, the effects of porosity and auxeticity have been investigated. Li et al. [9] studied the mechanical response of porous FG plates based on first-order shear deformation theory and isogeometric analysis. Gao et al. [13] developed a mathematical model to study wave propagation in graphene platelets-reinforced porous FG plates integrated with piezoelectric actuators and sensor layers. Akbas et al. [14] analysed the dynamic response of thick

FG porous sandwich beams using the 2D plane stress finite element method. Ramteke et al. [15] investigated the nonlinear eigenfrequency characteristics of the doubly curved multi-directional FG porous panels by using the finite element method (FEM). Wu et al. [16] analysed the free and forced vibrations of porous beams using FEM. Chen et al. [17] studied the static and dynamic properties of a porous beam.

Besides the FEM approaches, isogeometric analysis (IGA), originally established by Hughes et al. [18], is also used to study FG porous structures, especially when dealing with complex geometries such as "triply periodic minimal surface (TPMS)". In IGA, the same non-uniform rational B-splines (NURBS) basis functions that are used to model the exact geometry will be implemented to approximate the FE solution.
Nguyen-Xuan et al. [19] proposed an approach based on IGA and higher-order shear deformation theory (HSDT) to study the functionally graded TPMS plate. The use of higher-order shear deformation theories is to capture the nonlinear distribution of shear terms through the thickness of the plate and satisfy the zero-shear strains/stresses without using shear correction factors.
The approach is further extended to study graphene platelets-reinforced FG TPMS [20]. In another recent work, Nguyen et al. [21] have integrated non-local strain gradient with IGA to enable the consideration of softening and hardening and size-dependent phenomena in micro/nanostructures.
Another approach to increasing the accuracy of the results and the ability to capture microstructural features is to use generalised continua where additional degrees of freedom are endowed to each material point in addition to the standard displacement. In micropolar theory as an important category of generalised continua, the rotation of the material point is introduced as the additional degree of freedom, which is called microrotation to be distinguished from macro-rotation (local rigid rotation). Micropolar theory, also known as Cosserat, represents a significant advancement in the field of continuum mechanics, particularly in the modelling of materials that exhibit complex behaviours not adequately described by classical theories. This theory was first introduced by E. and F. Cosserat [22] and has since evolved by C. Eringen [23], [24], and W. Nowacki [25] to address various applications in engineering and materials science. W. Nowacki and C. Eringen have significantly shaped the understanding of this advanced theoretical framework. Eringen's work explored the concept of micro-polar elasticity and provided a robust mathematical framework that has been widely adopted in various fields [26]. Nowacki further enriched this theory by studying its implications in dynamic systems and wave propagation [27]. Elastic micropolar theory has been successfully used in many applications [28], [29] to describe heterogeneous materials [30], such as porous materials [31], [32], [33], [34], [35], cellular materials [36], composites [37], [38], lattices [39], foams [40], [41], [42], and even nanostructures [43], [44].

In the current literature, to study the structures with FG porosities, classical Cauchy continuum and non-local higher-order theories such as strain gradient theory are implemented. In these studies, the relative density is commonly taken as the dominant factor, and the relation between the elastic modulus and the density originally stems from a direct FEM calculation [45] or a micromechanics estimation [46], such as the modified rule of mixture [47] and Halpin Tsai [48] or available experiments [49].

In the present study, we advance this field by integrating non-classical micropolar theory to model porous plates that have in-plane functionally graded porosities. Compared to classical Cauchy theory, micropolar theory can better contemplate the internal structure of cellular solids [50] as it uses field description at the coarse level and preserves the memory of the material underlying structure at the fine level through internal scale parameters [44], [51], [52]. In this study, a homogenisation scheme is proposed based on the strain energy equivalence to determine the material constants of the equivalent continuum where the material parameters can consider the effect of both the size and shape of the pores. The collected data for various porosities determines the function for each material parameter in terms of the pore dimensions. Further, using the established homogenised model, the mechanical response of porous plates with various porosity distributions and a broad range of aspect ratios is investigated.

From a computational perspective, this study contributes by implementing a custom finite element method using the weak form of partial differential equations (PDE) in COMSOL Multiphysics to solve the micropolar elasticity problem. This is a notable advancement, as commercial FEM software typically does not support micropolar elasticity by default. Our custom formulation allows for the simulation of complex boundary conditions and loading scenarios, offering more precise predictions of mechanical responses. Additionally, the homogenisation scheme employed reduces computational complexity, enabling the study of large-scale porous structures without the burden of directly simulating their intricate microstructures. The combination of micropolar theory with advanced FEM not only enhances the computational efficiency but also provides a more accurate comparative analysis with classical Cauchy models, further underscoring the advantages of non-classical theories for FG porous materials.

To show the applicability of the proposed framework, it is implemented to design a biomedical prothesis used in dentistry called guided bone regeneration (GBR) mesh. GBR meshes are used in dentistry as mechanical barriers to isolate and protect the area of bone loss from the surrounding tissue while allowing new bone growth (Fig. 1***a***). While various types of barriers have been used for GBR, the design and mechanical properties of the GBR mesh can greatly influence its effectiveness in promoting bone growth [53]. GBR meshes are designed to be porous to facilitate the diffusion of fluids, oxygen, nutrients, and bioactive substances for cell growth, and an appropriate pore size can ensure the desirable occlusivity of the GBR membrane [54], [55].

To implant GBR meshes, they are fixed to the underneath mandible bone using biocompatible screws (Fig. 1***b***). Since these screws are located in critical loading areas, higher stiffness is required in the corresponding locations on the GBR mesh, and therefore, smaller pore sizes are more desirable. The importance of improving stiffness near fixing areas becomes more crucial when using biodegradable resorbable materials made of natural or synthetic polymers [56], such as PLA [57] or PLA composites [58]. The stiffness of these materials is much lower than that of metals like titanium alloy (Ti6Al4V) that are widely used in dentistry [59]. However, the use of bioresorbable materials is receiving great attention as it mitigates the need for a post-surgery to remove the GBR mesh after the bone regeneration process [60].

a. *b.*

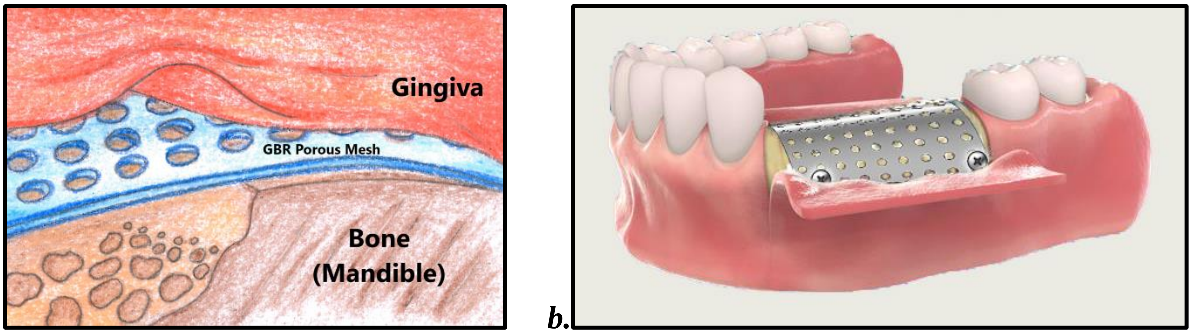

*Fig. 1**a.** Implementation of a porous GBR mesh **b.** Fixing GBR mesh to the underneath mandible bone using biocompatible screws*

On the other hand, bone has a heterogenous porous structure with microstructural features, for which non-classical micropolar models are proven to better describe microstructure-related scale effects on macroscopic effective properties [61], [62]. Lakes and co-workers [63], [64], [65], [66], [67] also conducted a series of experiments and studies on bones and found that micropolar theory provides better predictions of bone response than Cauchy elasticity. Such scale effects are most pronounced near bone-implant interfaces and in areas of high strain gradients [68]. In the current work, based on the developed framework, a design is suggested for the GBR mesh that can mimic the natural FG structure of the bone.

The remainder of this paper is structured as follows: Section 2 presents the homogenisation procedure implemented for extracting the equivalent material parameters for both micropolar and Cauchy continua. Section 3 describes the developed mechanical models for plates with an in-plane FG distribution of porosities. In Section 4, the obtained models are used to study the mechanical response of FG porous plates with different distributions of porosities. The findings are compared to the response of the detailed porous structure for a wide range of aspect ratios. The approach is used to propose an FG design for a dental GBR mesh in Section 5. Finally, Section 6 summarises the key findings and outlines future research directions in the field of porous FG structures.

2 Homogenisation

For modelling the FG porous plates with different microstructures (pore patterns), a multiscale approach [5] is proposed in which an equivalent homogenised material represents the porous heterogeneous structure. The equivalent model is described in the framework of both micropolar and classical (Cauchy) continua.

For the determination of the constitutive parameters of the equivalent models, the primary hypothesis is that the strain energy stored in the heterogeneous porous structure (micro-level) under prescribed boundary conditions is equal to that of the homogenous equivalent continuum description (macro-level). In the current work, at the micro-level, the classical Cauchy continuum is used, while at the macro-level, two different continuums (micropolar continuum and Cauchy continuum) are implemented, and the results are compared in describing FG porous structure (Fig. 2).

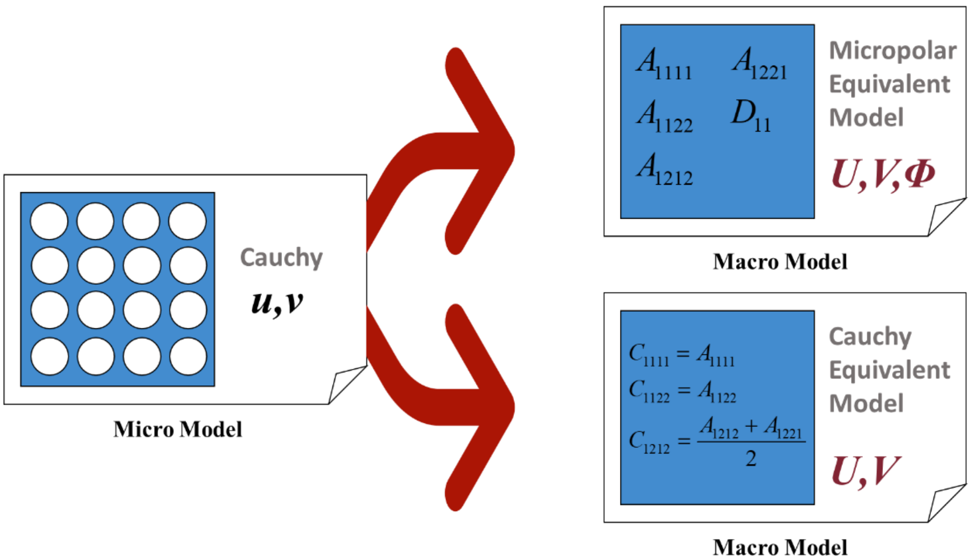

Fig. 2 The homogenisation procedure from classical Cauchy continuum at the micro-level to micropolar continuum and Cauchy continuum at the macro-level

The homogenisation procedure has been applied and thoroughly described before in [2]. For the sake of completeness, only the major equations are reported below. The homogenised constitutive parameters are further used in Section 3.2 to model functionally graded porous structures.

2.1 Homogenised Micropolar and Cauchy models

2.1.1 Micropolar Theory

The micropolar theory is governed by the following linearised kinematic equations:

$$\begin{aligned} \varepsilon_{ij} &= u_{i,j} + e_{ijk}\phi_k \\ \mu_{kj} &= \phi_{k,j} \end{aligned} \tag{1}$$

where u_i and ϕ_k stand for the components of displacement and micro-rotation vectors, ε_{ij} and μ_{kj} denote the components of strain and curvature tensors with e_{ijk} being the usual third-order permutation symbol.

If body forces (p_i) and body couples (q_k) are also considered, the equilibrium equations take the following form:

$$\begin{aligned} \sigma_{ij,j} + p_i &= 0 \\ \mu_{kj,j} - e_{ijk}\sigma_{ij} + q_k &= 0 \end{aligned} \tag{2}$$

Where σ_{ij} and μ_{kj} are the components of the non-symmetric stress and couple-stress tensors, respectively.

In the linearised 2D framework, there are two displacements and one rotational component that can be collected in the two following vectors:

$$\begin{aligned} \mathbf{u}^{\mathrm{T}} &= \begin{bmatrix} u & v \end{bmatrix} \\ \boldsymbol{\phi} &= \begin{bmatrix} \phi \end{bmatrix} \end{aligned} \tag{3}$$

and the strain and curvature vectors will be:

$$\boldsymbol{\varepsilon}^T = \begin{bmatrix} \varepsilon_{11} & \varepsilon_{22} & \varepsilon_{12} & \varepsilon_{21} \end{bmatrix}$$
$$\boldsymbol{\kappa}^T = \begin{bmatrix} \kappa_1 & \kappa_2 \end{bmatrix} \tag{4}$$

Where $\varepsilon_{11}, \varepsilon_{22}, \varepsilon_{12}, \varepsilon_{21}$ are the in-plane normal and shear strains, and κ_1, κ_2 are the micropolar curvatures.

The stress and couple stress vectors are also represented as:

$$\boldsymbol{\sigma}^T = \begin{bmatrix} \sigma_{11} & \sigma_{22} & \sigma_{12} & \sigma_{21} \end{bmatrix}$$
$$\boldsymbol{\mu}^T = \begin{bmatrix} \mu_1 & \mu_2 \end{bmatrix} \tag{5}$$

where σ_{ij} $(i, j = 1{,}2)$ represents the normal ($i = j$) and shear stress ($i \neq j$) components, and μ_1, μ_2 are the couple stresses or micro-couples.

The micropolar anisotropic constitutive equations can be represented as:

$$\begin{bmatrix} \boldsymbol{\sigma} \\ \boldsymbol{\mu} \end{bmatrix} = \boldsymbol{C} \begin{bmatrix} \boldsymbol{\varepsilon} \\ \boldsymbol{\kappa} \end{bmatrix} \tag{6}$$

where **C** is the constitutive stiffness matrix, which due to hyperelasticity is symmetrical [69]. The geometries considered here for the 2D periodic porous model (such as the one shown in Fig. 2) are symmetric with respect to a 90° rotation. These symmetries in the 2D model imply a special kind of orthotropic structure named "ortho-tetragonal" [37]. For the equivalent homogenised ortho-tetragonal material, the constitutive equations can be presented in Voigt's notation as:

$$\begin{bmatrix} \sigma_{11} \\ \sigma_{22} \\ \sigma_{12} \\ \sigma_{21} \\ \mu_1 \\ \mu_2 \end{bmatrix} = \begin{bmatrix} A_{1111} & A_{1122} & 0 & 0 & 0 & 0 \\ A_{1122} & A_{1111} & 0 & 0 & 0 & 0 \\ 0 & 0 & A_{1212} & A_{1221} & 0 & 0 \\ 0 & 0 & A_{1221} & A_{1212} & 0 & 0 \\ 0 & 0 & 0 & 0 & D_{11} & 0 \\ 0 & 0 & 0 & 0 & 0 & D_{11} \end{bmatrix} \begin{Bmatrix} \varepsilon_{11} \\ \varepsilon_{22} \\ \varepsilon_{12} \\ \varepsilon_{21} \\ \kappa_1 \\ \kappa_2 \end{Bmatrix} \tag{7}$$

2.1.2 Identification of Equivalent Micropolar Material Parameters

Since micropolar and Cauchy continua use different degrees of freedom, a kinematic map is required to link the two levels of description. Here, we followed the mapping proposed by Forest and Sab [30] for a square representative volume element (RVE).

$$u^* = \varepsilon_{11} x + \varepsilon_{12}^{SYM} y - \frac{\kappa_2}{2} y^2 - \kappa_1 xy - \frac{10}{L^2}\theta(y^3 - 3yx^2)$$
$$v^* = \varepsilon_{12}^{SYM} x + \varepsilon_{22} y + \frac{\kappa_1}{2} x^2 - \kappa_2 xy + \frac{10}{L^2}\theta(x^3 - 3xy^2) \tag{8}$$

Eq. (8) expresses the approximate microscopic displacement field within the RVE (u^*, v^*) as a function of the macroscopic strain measures ($\varepsilon_{11}, \varepsilon_{22}, \varepsilon_{12}^{SYM}, \theta, \kappa_1, \kappa_2$) at the material point on the macro-level.

After determination of the kinematic map, to find the micropolar material parameters in Eq. (7), first we calculate the response of the porous plate subjected to various loadings using FEM. In each case, the corresponding micropolar material parameters are found so that the equivalent material stores the same strain energy density when subjected to the identical loading, i.e.,

$$U_{FEM} = U_{Micropolar} \tag{9}$$

Where $U_{Micropolar}$ is the strain energy density of the equivalent micropolar continuum calculated using the following relation:

$$\begin{aligned} U_{Micropolar} &= \frac{1}{2}\left[\varepsilon_{11}\sigma_{11} + \varepsilon_{22}\sigma_{22} + \varepsilon_{12}^{SYM}\sigma_{12}^{SYM} + \theta\sigma_{12}^{ASM} + \kappa_1\mu_1 + \kappa_2\mu_2\right] \\ &= \frac{1}{2}[\varepsilon_{11}(A_{1111}\varepsilon_{11} + A_{1122}\varepsilon_{22}) + \varepsilon_{22}(A_{1122}\varepsilon_{11} + A_{1111}\varepsilon_{22}) + \\ &\quad \varepsilon_{12}^{SYM}(\frac{A_{1212} + A_{1221}}{2}\varepsilon_{12}^{SYM}) + \theta(\frac{A_{1212} - A_{1221}}{2}\theta) \quad + \\ &\quad \kappa_1(D_{11}\kappa_1) + \kappa_2(D_{11}\kappa_2)] \end{aligned} \tag{10}$$

And U_{FEM} is the strain energy density of the porous plate calculated using the finite element method:

$$U_{FEM} = \frac{1}{2}\int_{RVE} \sigma_{ij}^{p}\varepsilon_{ij}^{p}dV \tag{11}$$

Where σ_{ij}^{p} and ε_{ij}^{p} are stress and strain in the porous structure.

To evaluate the components of the micropolar stiffness tensor ($A_{1111}, A_{1122}, A_{1212}, A_{1221}, D_{11}$), different boundary conditions are designed to represent uniaxial, biaxial, symmetric shear, bending, and rotational deformations. The applied tests, the corresponding material parameters obtained from each test, and the applied boundary conditions are described in Fig. 3. The boundary conditions to create each test are obtained using the micro-filed descriptions u^*, v^* in terms of macro-field strain measures presented in the kinematic map, i.e., Eq. (8).

Test 1 Uniaxial	Test 2 Biaxial	Test 3 Symmetric Shear	Test 4 Rotation	Test 5 Curvature
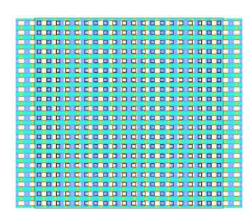	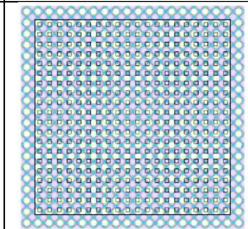	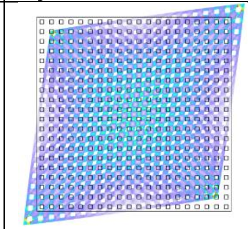	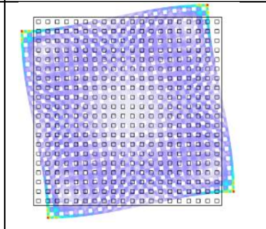	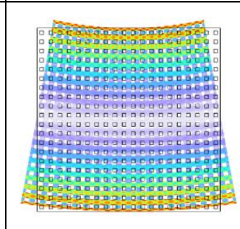
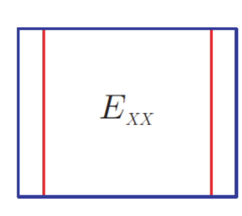 E_{XX}	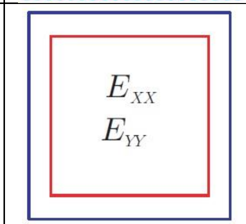 E_{XX} E_{YY}	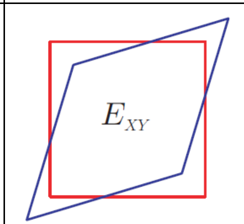 E_{XY}	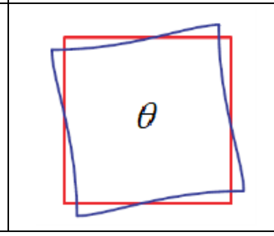 θ	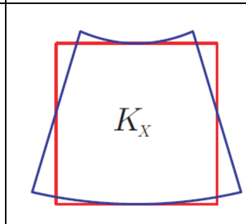 K_X
A_{1111}	A_{1122}	A_{1212}, A_{1221}		D_{11}
$u^* = x$ $v^* = 0$	$u^* = x$ $v^* = y$	$u^* = y$ $v^* = x$	$u^* = \frac{10}{L^2}\left(y^3 - 3yx^2\right)$ $v^* = \frac{10}{L^2}\left(3xy^2 - x^3\right)$	$u^* = -x\,y$ $v^* = \frac{x^2}{2}$

Fig. 3 Designed FEM tests for finding micropolar material parameters.

More details on how to apply the boundary conditions and calculate each parameter can be found in [2].

To find the homogenised Cauchy model, an analogous approach is followed in the framework of Cauchy theory, which requires the definition of only three constitutive components. In this case, the homogenisation is straightforward because there is no need to define a kinematic map. Alternatively, such properties can be deducted from the micropolar one [70].

2.2 Finite Element Model

The finite element implementation at both macro (micropolar) and microlevels (Cauchy) is described in this section. Since commercial FE codes do not yet support the micropolar continuum, we implement the weak form of partial differential equations (PDE) numerically in COMSOL Multiphysics. By using PDE modelling in COMSOL instead of traditional FE modelling, no user subroutines are required and various complex geometries, boundary conditions, and loadings can be applied in a user-friendly graphical interface.

Regarding meshing and discretisation, the porous structure was discretised using first-order (linear) triangular elements. The thickness of the plate was assumed to be $W/100$, and therefore a 2D plane stress formulation for linear elastic media was adopted. The mesh of homogenous equivalent models is made of structured quadrilateral first-order (linear) elements. Note that the same approximation order for both displacements and micro-rotation were used.

The weak form is formulated based on the virtual work principle for a micropolar continuum with $\mathbf{u}$ and $\boldsymbol{\phi}$ as a set of kinematically admissible displacement and rotation fields, such that:

$$\int_{\Omega} \delta\boldsymbol{\varepsilon}^T \boldsymbol{\sigma}\, d\Omega + \int_{\Omega} \delta\boldsymbol{\kappa}^T \boldsymbol{\mu}\, d\Omega = \int_{\Omega} \delta\boldsymbol{u}^T \boldsymbol{p}\, d\Omega + \int_{B} \delta\boldsymbol{u}^T \boldsymbol{t}\, dB + \int_{\Omega} \delta\boldsymbol{\phi}^T \boldsymbol{q}\, d\Omega + \int_{B} \delta\boldsymbol{\phi}^T \boldsymbol{m}\, dB, \ \ \forall \delta\boldsymbol{u}, \delta\boldsymbol{\phi} \tag{12}$$

Where Ω is the entire computational domain, δ denotes the variational operator with $\boldsymbol{t}$ and $\boldsymbol{m}$ the traction and couple-traction vectors applied on the boundary B.

Displacement and microrotations are approximated by interpolating the nodal values $\tilde{\boldsymbol{u}}$ and $\tilde{\boldsymbol{\phi}}$, considered primal unknowns, using the shape functions as follows:

$$\boldsymbol{u} = \boldsymbol{N}_u \tilde{\boldsymbol{u}}, \quad \boldsymbol{\phi} = \boldsymbol{N}_\varphi \tilde{\boldsymbol{\phi}} \tag{13}$$

For quadrilateral elements, with first-order (linear) discretisation for both displacements and micro-rotation, the shape function matrices will be:

$$\begin{aligned} \boldsymbol{N}_u &= \begin{bmatrix} N_1 & 0 & N_2 & 0 & N_3 & 0 & N_4 & 0 \\ 0 & N_1 & 0 & N_2 & 0 & N_3 & 0 & N_4 \end{bmatrix} \\ \boldsymbol{N}_\varphi &= \begin{bmatrix} N_1 & N_2 & N_3 & N_4 \end{bmatrix} \end{aligned} \tag{14}$$

Also, the micropolar strains and curvatures given in Eq. (1) can be written as:

$$\begin{aligned} \boldsymbol{\varepsilon} &= \boldsymbol{L}\boldsymbol{u} + \boldsymbol{M}\boldsymbol{\phi} \\ \boldsymbol{\kappa} &= \nabla\boldsymbol{\phi} \end{aligned} \tag{15}$$

Where ∇ is the gradient operator in the 2D framework, and $\boldsymbol{L}$ and $\boldsymbol{M}$ are:

$$\boldsymbol{L} = \begin{bmatrix} \dfrac{\partial}{\partial x} & 0 & \dfrac{\partial}{\partial y} & 0 \\ 0 & \dfrac{\partial}{\partial y} & 0 & \dfrac{\partial}{\partial x} \end{bmatrix}^T, \quad \boldsymbol{M} = \begin{bmatrix} 0 \\ 0 \\ +1 \\ -1 \end{bmatrix} \tag{16}$$

By substituting Eq. (13) in Eq. (15), we have:

$$\begin{aligned} \boldsymbol{\varepsilon} &= \boldsymbol{L}\boldsymbol{N}_u \tilde{\boldsymbol{u}} + \boldsymbol{M}\boldsymbol{N}_\varphi \tilde{\boldsymbol{\phi}} = \begin{bmatrix} \boldsymbol{L}\boldsymbol{N}_u & \boldsymbol{M}\boldsymbol{N}_\varphi \end{bmatrix} \begin{Bmatrix} \tilde{\boldsymbol{u}} \\ \tilde{\boldsymbol{\phi}} \end{Bmatrix} = \boldsymbol{B}_\varepsilon \boldsymbol{d} \\ \boldsymbol{\kappa} &= \nabla\boldsymbol{N}_\varphi \tilde{\boldsymbol{\phi}} = \begin{bmatrix} 0 & \nabla\boldsymbol{N}_\varphi \end{bmatrix} \begin{Bmatrix} \tilde{\boldsymbol{u}} \\ \tilde{\boldsymbol{\phi}} \end{Bmatrix} = \boldsymbol{B}_\kappa \boldsymbol{d} \end{aligned} \tag{17}$$

Where $\boldsymbol{d}$ is the unknown vector of nodal displacements and the matrices $\boldsymbol{B}_\varepsilon$ and $\boldsymbol{B}_\kappa$ contains the derivatives of shape functions.

The constitutive matrix for 2D ortho-tetragonal micropolar material in Eq. (7) will then become:

$$\boldsymbol{\sigma} = \boldsymbol{D}_\varepsilon \boldsymbol{B}_\varepsilon \boldsymbol{d} \quad \boldsymbol{\mu} = \boldsymbol{D}_\kappa \boldsymbol{B}_\kappa \boldsymbol{d} \tag{18}$$

Where:

$$\boldsymbol{D}_{\varepsilon}=\begin{bmatrix} A_{1111} & A_{1122} & 0 & 0 \\ A_{1122} & A_{1111} & 0 & 0 \\ 0 & 0 & A_{1212} & A_{1221} \\ 0 & 0 & A_{1221} & A_{1212} \end{bmatrix}, \quad \boldsymbol{D}_{\kappa}=\begin{bmatrix} D_{11} & 0 \\ 0 & D_{11} \end{bmatrix} \tag{19}$$

In the absence of body forces and couples, the algebraic finite element problem reads:

$$\delta \boldsymbol{d}^{T} \underbrace{\int_{\Omega} (\boldsymbol{B}_{\varepsilon}^{T}\boldsymbol{D}_{\varepsilon}\boldsymbol{B}_{\varepsilon}+\boldsymbol{B}_{\kappa}^{T}\boldsymbol{D}_{\kappa}\boldsymbol{B}_{\kappa})d\Omega}_{\boldsymbol{K}} = \delta \boldsymbol{d}^{T} \underbrace{\int_{B} \begin{bmatrix} \boldsymbol{N}_{u}^{T}\boldsymbol{t} \\ \boldsymbol{N}_{\phi}^{T}\boldsymbol{m} \end{bmatrix} dB}_{\boldsymbol{F}}, \forall \delta \boldsymbol{d} \tag{20}$$

Where $\boldsymbol{K}$ and $\boldsymbol{F}$ indicate the elemental stiffness matrix and the nodal force vector.

The elemental stiffness matrix $\boldsymbol{K}$ is then assembled into the global stiffness matrix, $\boldsymbol{K}_{Global}$, by summing contributions from all elements and aligning the global degree of freedoms:

$$\boldsymbol{K}_{Global}\begin{Bmatrix} \boldsymbol{U} \\ \boldsymbol{\Phi} \end{Bmatrix} = \begin{Bmatrix} \boldsymbol{T} \\ \boldsymbol{M} \end{Bmatrix} \tag{21}$$

Where $\boldsymbol{U}$ and $\boldsymbol{\Phi}$ are the global displacement and microrotation vectors, and $\boldsymbol{T}$ and $\boldsymbol{M}$ are the global force and moment vectors.

For the benefit of readers, we also present how to practically implement the weak form of the equations in the COMSOL PDE framework.

We start from the balance equations and multiply each of them by its corresponding test functions, denoted here as u_i^{test} and ϕ_k^{test}, and integrate over the entire computational domain *D.*

$$\int_{\Omega} (\sigma_{ij,j}u_i^{test} + p_i u_i^{test})\, d\Omega + \int_{\Omega} (\mu_{kj,j} - e_{ijk}\sigma_{ij} + q_k)\phi_k^{test} d\Omega = 0 \tag{22}$$

It should be noted that the test functions are inherently the virtual displacement introduced previously in Eq. (12).

By applying the divergence theorem and considering *B* as the surface boundary, the weak form equations can be defined:

$$\begin{aligned} &(-\int_{\Omega} \sigma_{ij}u_{i,j}^{test}\, d\Omega + \int_{B} \sigma_{ij}u_i^{test}n_j\, dB + \int_{\Omega} p_i u_i^{test}\, d\Omega) + \\ &(-\int_{\Omega} \mu_{kj}\phi_{k,j}^{test}\, d\Omega + \int_{B} \mu_{kj}\phi_k^{test}n_j\, dB - \int_{\Omega} e_{ijk}\sigma_{ij}\phi_k^{test}\, d\Omega + \int_{\Omega} q_k\phi_k^{test}\, d\Omega) = 0 \end{aligned} \tag{23}$$

Where the domain and surface contributions can be rearranged as:

$$\int_{\Omega}(-\sigma_{ij}u_{i,j}^{test}+p_i u_i^{test}-\mu_{kj}\phi_{k,j}^{test}-e_{ijk}\sigma_{ij}\phi_k^{test}+q_k\phi_k^{test})d\Omega$$
$$+\int_{B}(\sigma_{ij}u_i^{test}n_j+\mu_{kj}\phi_k^{test}n_j)dB=0 \qquad (24)$$

In PDE COMSOL, the domain contribution specifies the governing equations, while the surface contribution should be defined in weak form as the boundary conditions. This is the main leverage of implementing micropolar theory through the PDE framework developed in the current work: By properly defining the weak form of governing equations and boundary conditions, constitutive equations, and kinematic relations, one can benefit from the developed capacity of COMSOL for discretisation, definition of shape functions, as well as derivation and assemblage of stiffness matrix.

3 Functionally graded porous plates

3.1 Geometrical Modelling

Consider a porous rectangular plate with length *L*, width *W*, and height (thickness) *h*, as presented in Fig. 4.

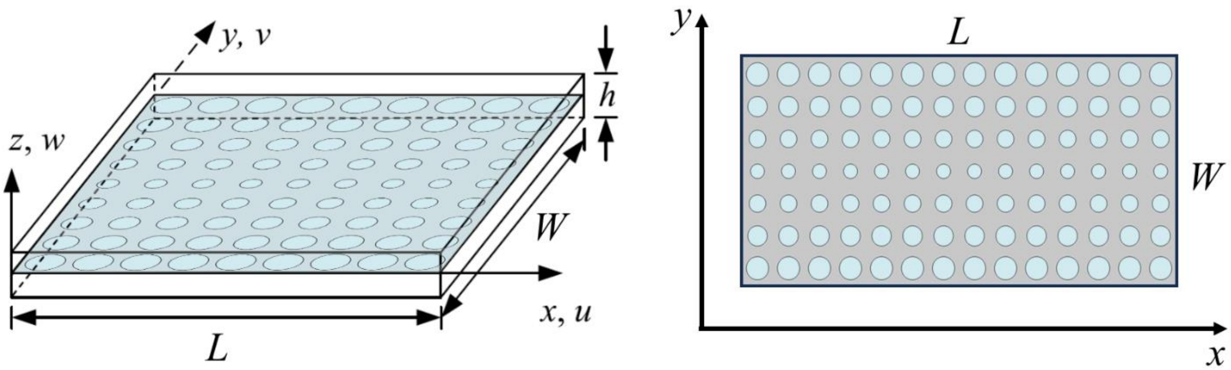

Fig. 4 The coordinates and geometry of the porous rectangle plate and the 2D model

The Cartesian coordinates (*x*, *y*, *z*), located in the mid-plane, are used to define the displacements *u*, *v*, and *w* in the length, width, and thickness directions. The porosity distributions can occur in the in-plane directions, such as *x*-direction and *y*-direction, as well as the thickness [71]. Four different kinds of porosity distributions in the *y*-direction (Types 'V', 'A', 'X', and 'O', see Fig. 5), which are standard in the literature [48], are used here to study the mechanical behaviour of the FG porous plate.

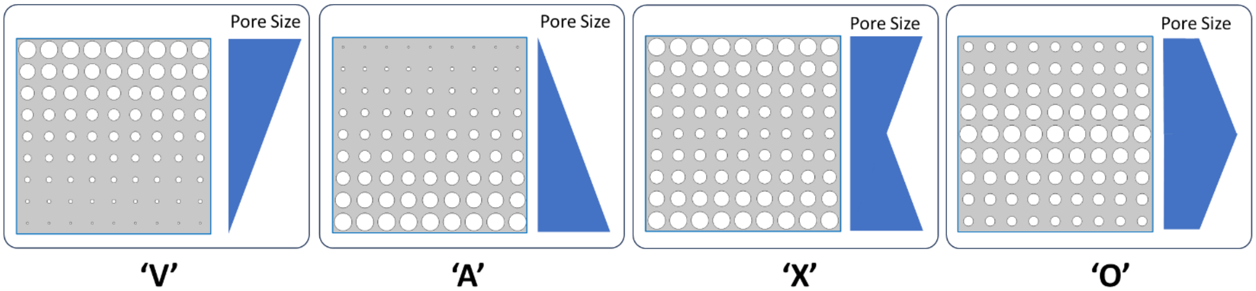

Fig. 5 Four different types of porosity distribution through the in-plane y-direction

For type 'V', the porosity distribution is linearly varied in the y-direction from a small pore size of 0.01 W at y = 0 to the pore size of 0.09 W at y = W. Therefore, the maximum and minimum values of effective stiffness parameters correspond to the bottom and the top surfaces, respectively. For type 'A', the porosity distribution linearly varies in the y-direction from a pore size of 0.09 W at y = 0 to the pore size of 0.01 W at y = W. Therefore, contrary to the type 'V', the minimum and maximum values of effective stiffness parameters correspond to the bottom and the top surfaces, respectively. Type 'X' consists of two piecewise linear parts where the smallest pore size is located on the midline and the largest size on the top and bottom parts. Reversely to type X, for type 'O', the largest pore size is located on the midline and the smallest size on the top and bottom parts. Various porosity distributions can be considered as a function of vertical location (y). The variation of the pore size through the FG structure for the four porosity distributions in the current work is represented in Fig. 6.

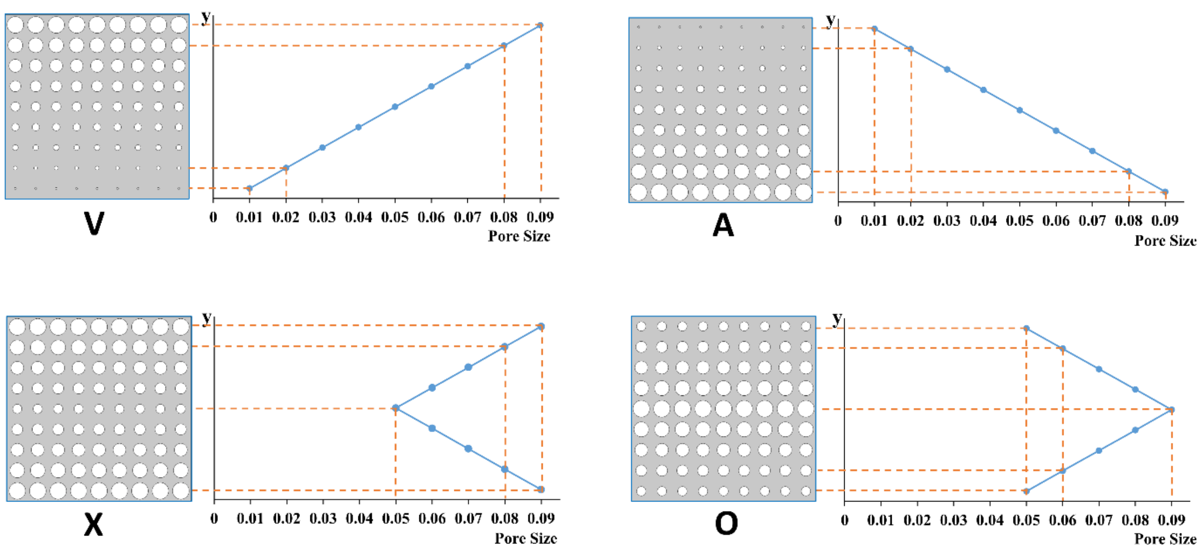

Fig. 6 The variation of pore sizes through height for each porosity distribution

Based on the distribution of porosity, the variation of the pore size (l_p) along the y direction can be described as $l_p = g_*(y)$ where the subscript $*$ refers to the type of porosity distribution. Considering the minimum pore size as 0.01 W and the maximum as 0.09 W, the functions for each type of porosity distribution are as follows:

$$
\begin{aligned}
l_p &= g_V(y) = \frac{0.09}{W} y + 0.05 \quad (V) \\
l_p &= g_A(y) = -\frac{0.09}{W} y + 0.05 \quad (A) \\
l_p &= g_X(y) = \frac{0.09}{W} |y| + 0.09 \quad (X) \\
l_p &= g_O(y) = -\frac{0.09}{W} |y| + 0.09 \quad (O)
\end{aligned} \tag{25}
$$

In which $|y|$ is the absolute (positive) value of the vertical position (y), and y origin is located at $W/2$.

3.2 Equivalent homogenised models for FG porous plates

Fig. 7 shows how the equivalent homogenised FG porous structure is derived by considering the homogenisation procedure developed for unit cells with uniform porosity [2]. First, a parametric study is conducted to find the equivalent mechanical parameters (Cauchy and micropolar) of uniform porous plates with various pore sizes. In the parametric study, the pore density (i.e., the number of pores per unit length) is kept constant and the pore sizes are changed from 0.01 W to 0.09 W to find the required equivalent parameters for each section of FG porous structure.

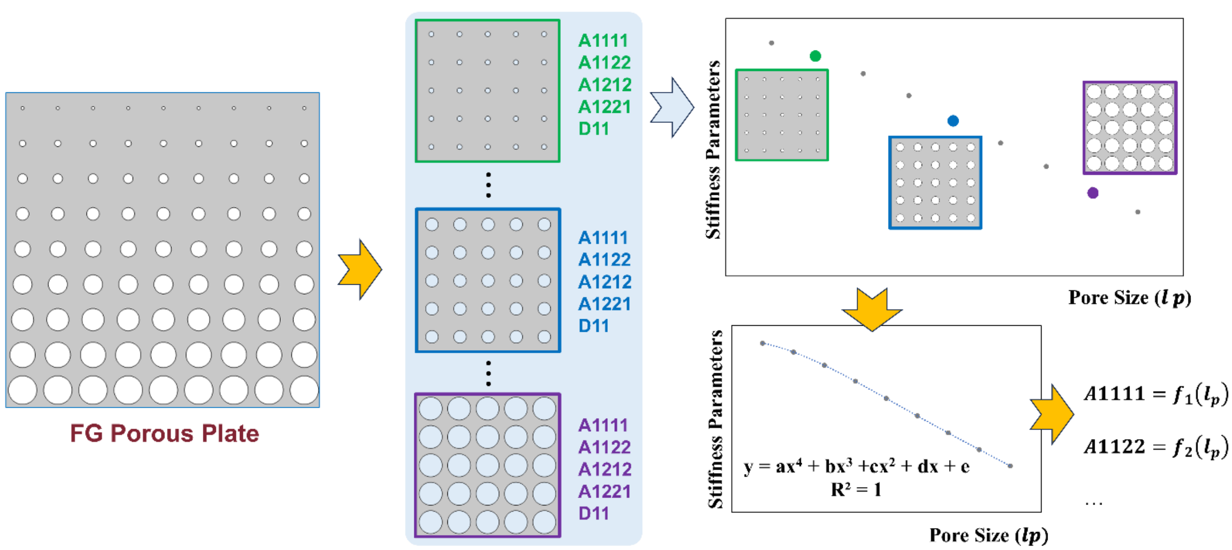

Fig. 7 A graphical abstract of the methodology for developing equivalent homogenised models of FG porous plates

The flowchart in Fig. 8 shows the overall algorithm and workflow of the present work.

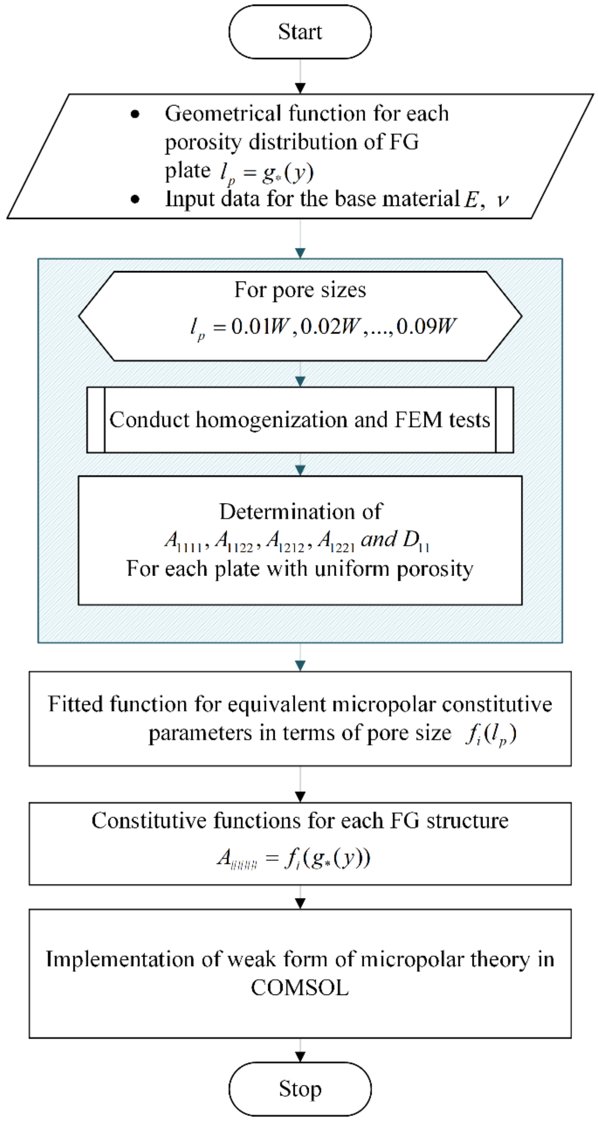

Fig. 8 The flowchart for the implementation algorithm of the present work

For studying the FG patterns, we choose the pore size to vary in the range of 0.01L to 0.09L. When the pore size exceeds 0.09L, the reduction of material thickness between the pores can lead to local buckling or instability under loading, which may not be fully captured by the homogenised model. Also, very small pore sizes less than 0.01L can pose challenges related to meshing and discretisation, particularly near the discontinuities, which may reduce the numerical accuracy.

In the applications, we consider polylactic acid (PLA) as base material of the porous plate. PLA is a biodegradable and non-toxic material that is approved by the FDA for bioresorbable medical implants and therefore is widely used in the biomedical sector [58], [72]. The material properties considered for PLA are listed in Table 1.

Table 1 Material properties of the base material (PLA) [57], [73]

Properties	Value	Unit

Young's Modulus	3.775	GPa
Poisson Ratio	0.3	-
Density	1120	kg/m^3

In Fig. 9, the equivalent micropolar and Cauchy parameters for the pore sizes ranging from 0.01W to 0.09W are presented.

These data are then utilised to find curve-fitted functions, $f_i(l_p)$, for each material parameter with respect to the pore size, l_p.

The obtained functions for equivalent constitutive parameters (in Pa) are as follows:

$$
\begin{aligned}
A_{1111} &= f_1(l_p) = -41264 l_p^{\,4} + 11339 l_p^{\,3} - 1107.1 l_p^{\,2} + 4.4412 l_p + 4.1318 \\
A_{1122} &= f_2(l_p) = -1152 l_p^{\,4} + 2240.8 l_p^{\,3} - 357.8 l_p^{\,2} + 3.1343 l_p + 1.2268 \\
A_{1212} &= f_3(l_p) = -21.30 l_p^{\,4} + 3013.50 l_p^{\,3} - 506.03 l_p^{\,2} + 2.26 l_p + 1.94 \\
A_{1221} &= f_4(l_p) = 7501.8 l_p^{\,4} + 926.53 l_p^{\,3} - 281.96 l_p^{\,2} + 2.2673 l_p + 0.9298 \\
D_{11} &= f_5(l_p) = -3355.3 l_p^{\,4} + 879.59 l_p^{\,3} - 83.344 l_p^{\,2} + 0.2526 l_p + 0.3249
\end{aligned} \tag{26}
$$

And the functions for equivalent constitutive parameters for Cauchy theory are those described in Eq. (13) for $C_{1111} = A_{1111}$, $C_{1122} = A_{1122}$ and $C_{1212} = (A_{1212} + A_{1221})/2$.

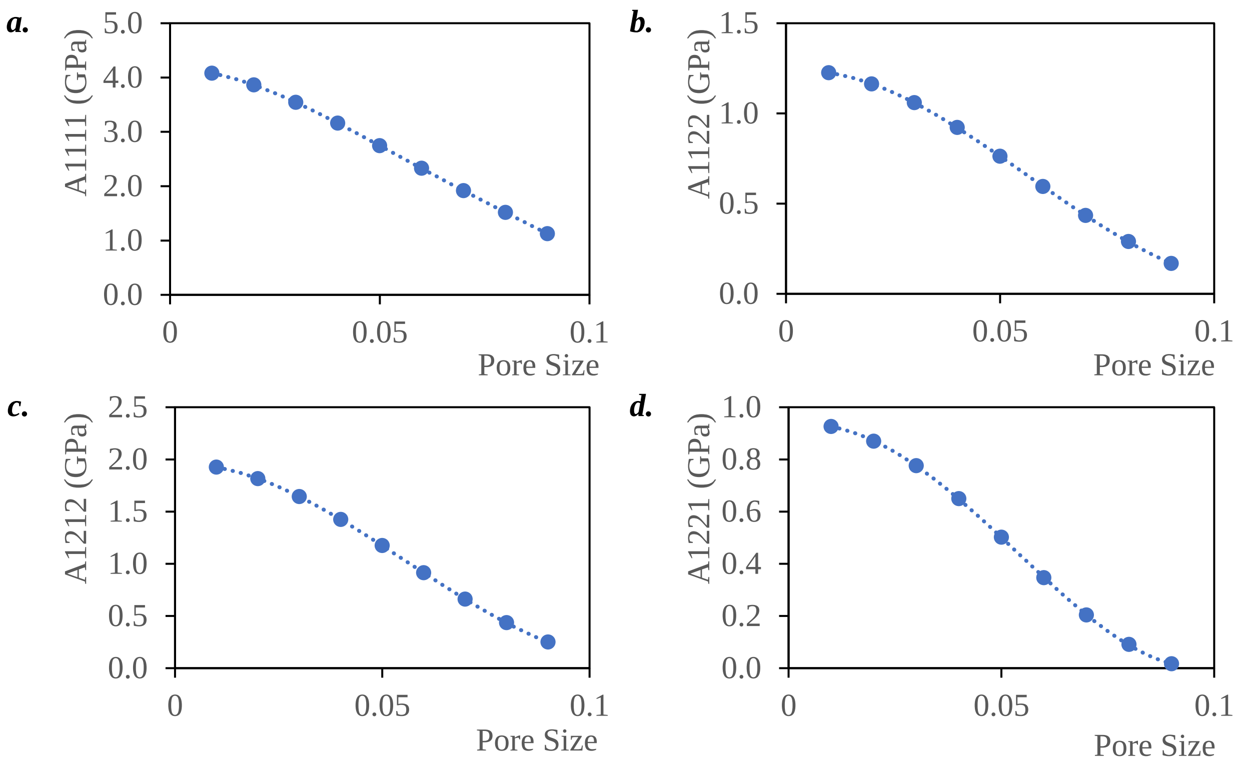

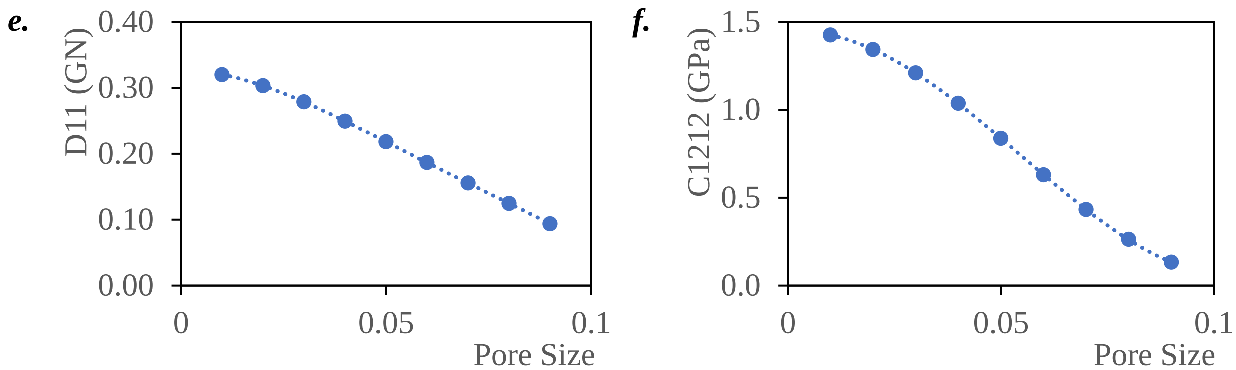

*Fig. 9 The equivalent micropolar (**a.-e.**) and Cauchy (**a.**, **b.**, and **f.**) material parameters for pore sizes ranging from 0.01W to 0.09W.*

Now, by considering the relationship between homogenised material parameters and pore sizes ($f_i(l_p)$) as well as the functionality of pore sizes versus locations ($l_p = g_*(y)$) in each FG porous pattern, it is possible to determine the constitutive functions for each FG structure by employing the composition operator:

$$A_{\#\#\#\#} = f_i(g_*(y)) \tag{27}$$

Where $A_{\#\#\#\#}$ represents the constitutive parameters of the homogenised micropolar/Cauchy model (see Eq. (26)).

4 Numerical Results and Discussion

4.1 Geometry, loading, and boundary conditions

The usefulness of micropolar model is more evident when concentrated forces are applied and/or geometric discontinuities are present [38]. Also, micropolar theory is more effective compared to the Cauchy theory when structures are intended to withstand shear loads as normal stiffness properties are the same between micropolar and Cauchy theories $C_{1111} = A_{1111}$ and $C_{1122} = A_{1122}$. Therefore, to evaluate the effectiveness of micropolar theory and its proficiency to Cauchy theory in describing the mechanical performance of FG porous structures, two loading scenarios are considered: a distributed shear load and a vertical indentation load. The distributed shear load is applied on the top surface of the porous plate/beam (p = 1000 N/m), while the bottom surface of the structure is fixed. Various length scales (L/W) were investigated for four types of porosity distributions by comparing the results for $L/W < 1$, $L/W = 1$, and $L/W > 1$ (Fig. 10). In all the structures, L is fixed as 1.

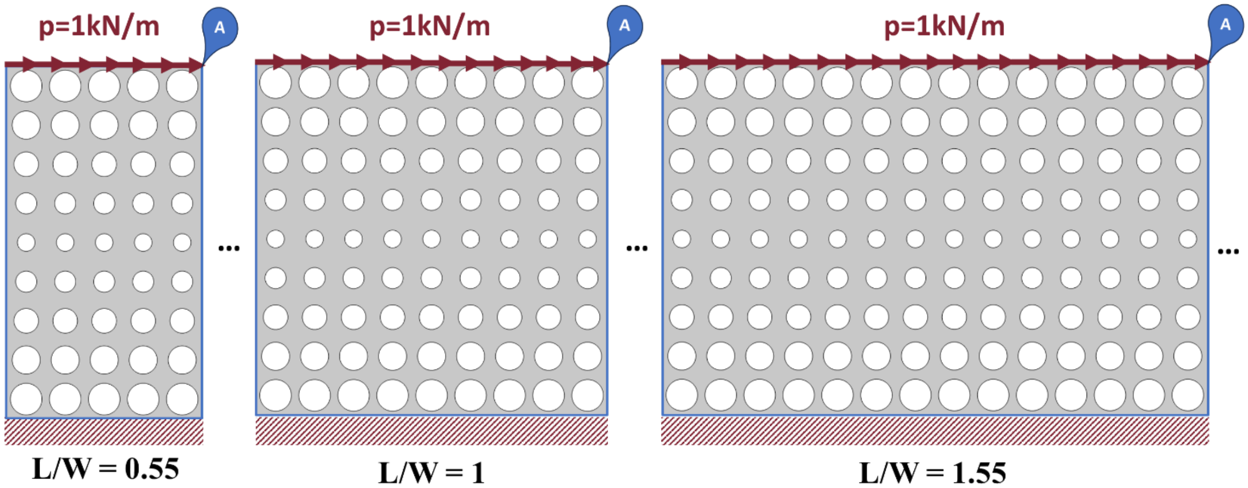

Fig. 10 The geometry and loading considered for evaluation of the mechanical response of porous plates. L is the length (horizontal length) and W is the width (vertical length).

4.2 Comparison of displacement distribution for porous and homogenised models

To get insight into the mechanical response within the plate, the normalised displacement on the midline ($y = W/2$) is compared for the porous model versus homogenised models while considering various porosity distributions. The effect of the three aspect ratios $L/W = 0.55$, $L/W = 1$, and $L/W = 1.55$ is also studied. All the displacements are normalised by L. The results are summarised in Fig. 11 for four types of porosity distributions: Types A, V, X, and O, respectively. Here, "DT", "MP" and "CHY" denote detailed porous models, micropolar homogenised models, and Cauchy homogenised models, respectively.

a.

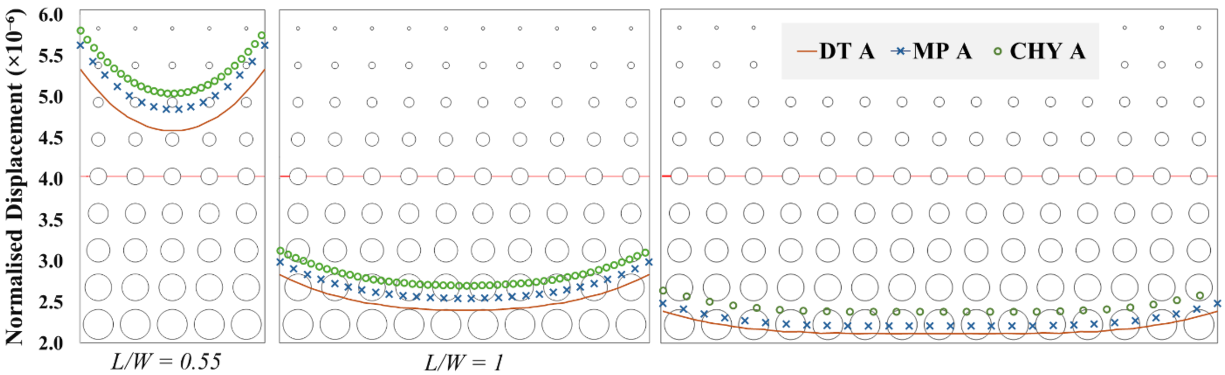
Normalised Displacement (×10⁻⁶)
6.0
5.5
5.0
4.5
4.0
3.5
3.0
2.5
2.0
DT A
MP A
CHY A
L/W = 0.55
L/W = 1

b.

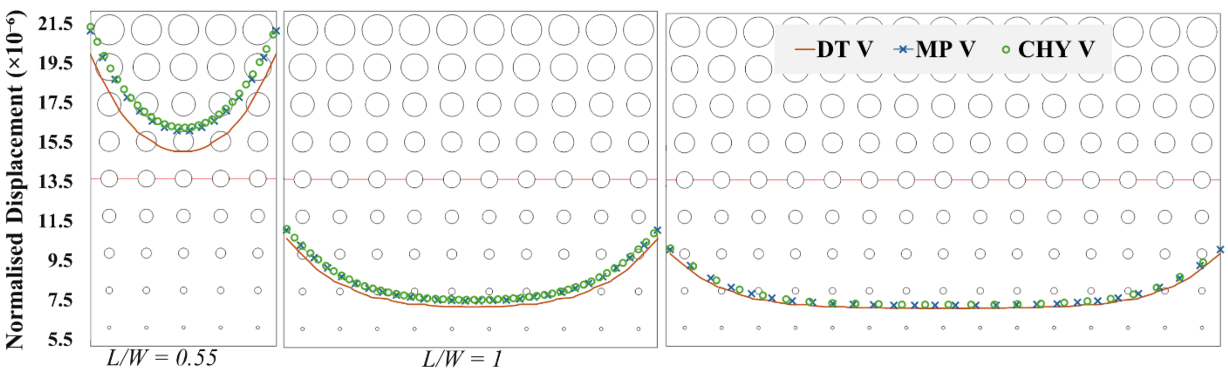
Normalised Displacement (×10⁻⁶)
21.5
19.5
17.5
15.5
13.5
11.5
9.5
7.5
5.5
DT V
MP V
CHY V
L/W = 0.55
L/W = 1

c.

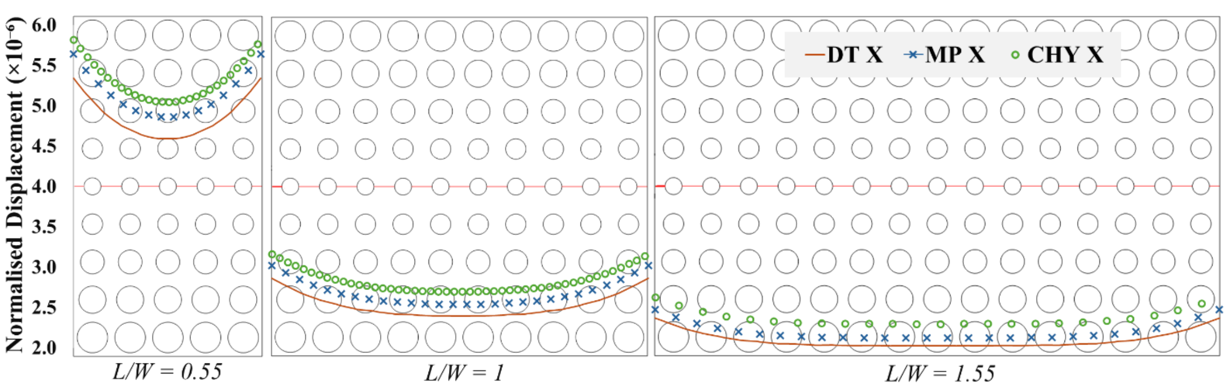
Normalised Displacement (×10⁻⁶)
6.0
5.5
5.0
4.5
4.0
3.5
3.0
2.5
2.0
DT X
MP X
CHY X
L/W = 0.55
L/W = 1
L/W = 1.55

d.

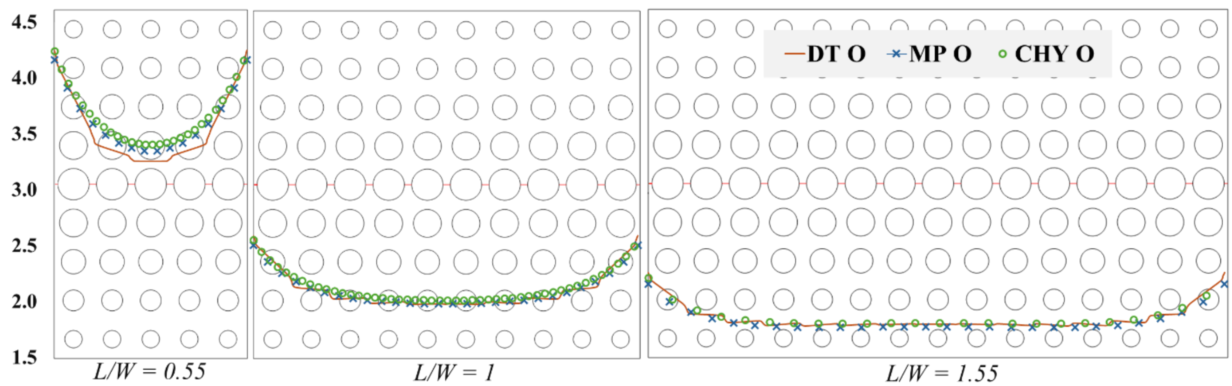

*Fig. 11 The comparison of the normalised displacement magnitude on the midline for the porous model versus homogenised micropolar and Cauchy models for FG porous structure with porosity distribution of **a.** Type A, **b.** Type V, **c.** Type X, **d.** Type O with aspect ratios of L/W = 0.55, L/W = 1, and L/W = 1.55.*

The results for the studied cases show that micropolar homogenised models can better predict the displacement distribution of the FG porous structure compared to the Cauchy homogenised model for all porosity patterns. The advantage of micropolar to Cauchy theory is more prominent in the case of A and X patterns.

In Fig. 12, the normalised displacement contour lines are compared for the case of $L/W = 1$ for all the four porosity patterns of types A, V, X, and O, respectively.

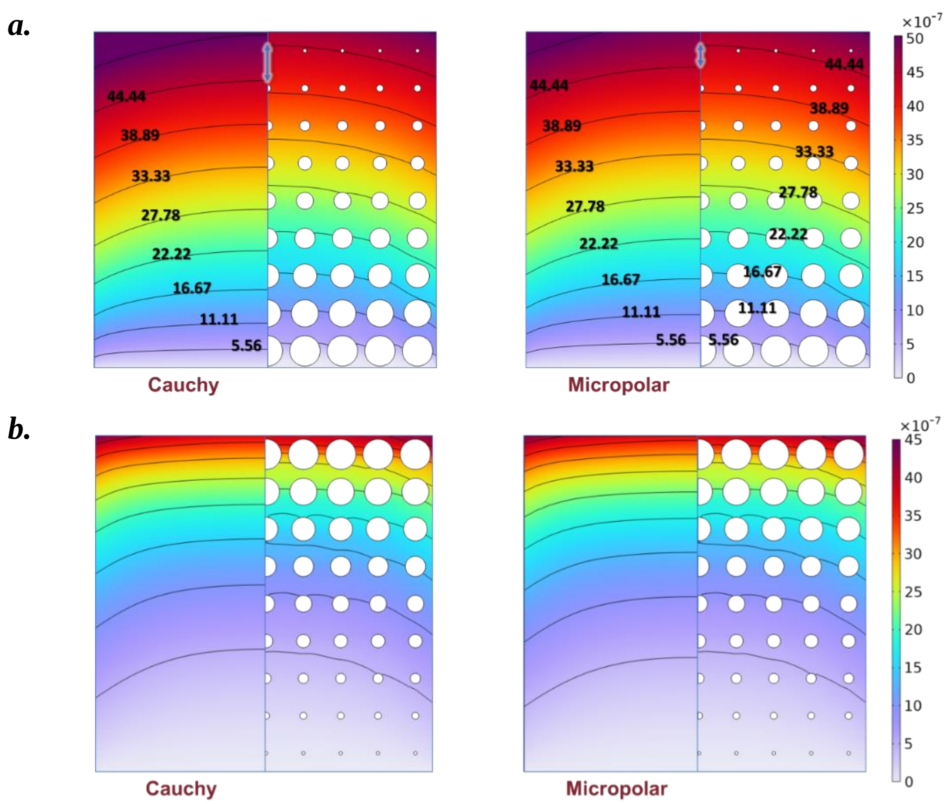

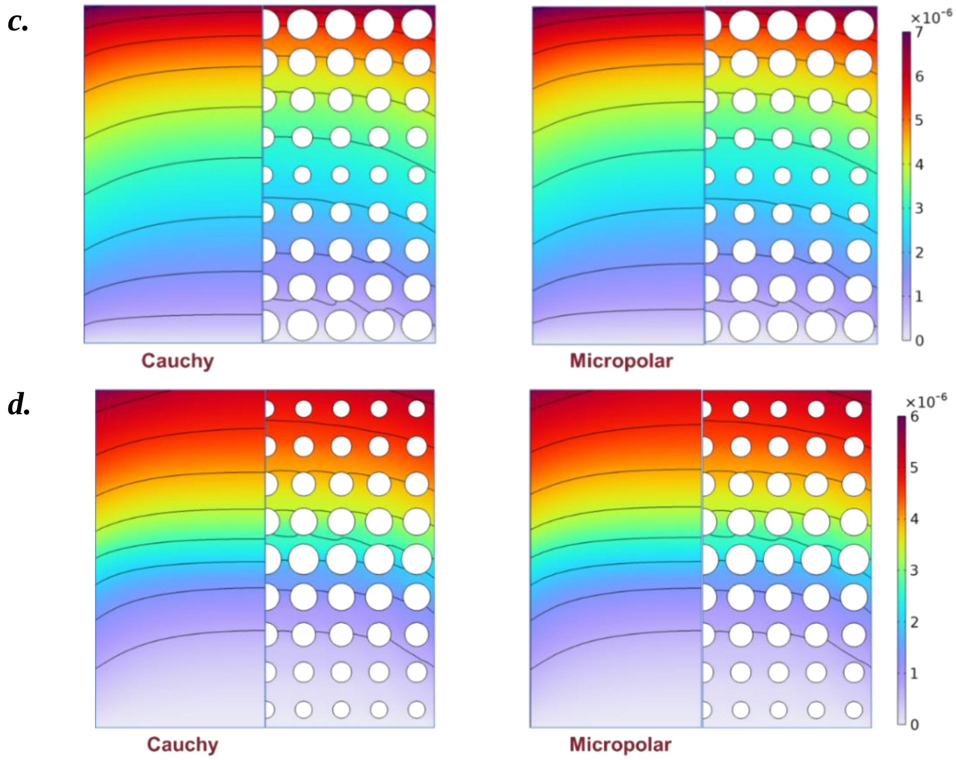

*Fig. 12 Comparison of normalised displacement contours of the porous model versus homogenised micropolar and Cauchy models for FG porous structure with porosity distribution **a.** Type A, **b.** Type V, **c.** Type X, **d.** Type O, and L/W = 1. The values of contour lines are reported in **a.** for better presentation of the differences.*

As shown in Fig. 12, both homogenised models can follow the displacement contours of the detailed porous model. In Fig. 12***a***, the arrows show the distance between the displacement iso-lines in the porous model and the corresponding predicted iso-line by each homogenised model. As it can be seen, the performance of the homogenised micropolar model is better as the displacement iso-lines are closer to the porous FG structures for the micropolar homogenised models compared to Cauchy ones.

4.3 Aspect ratio effect

To evaluate the aspect ratio effect on the stiffness of the porous structures and the capability of the homogenised models in predicting stiffness, the maximum deflection (normalised displacement at point A in Fig. 10) is compared for porous and equivalent micropolar and Cauchy models for 10 aspect ratios and the four FG patterns.

The results are presented in Table 2 and Fig. 13. Overall, the obtained results for homogenised micropolar and Cauchy models are consistent with the porous model. However, according to Table 2, compared to Cauchy theory, the micropolar model better predicts the mechanical behaviour of porous structures, especially for very small aspect ratios such as AR = 0.55. As aspect ratio increases, the difference between the porous response and micropolar prediction decreases.

Table 2 Comparison of the normalised displacement magnitude (in μ) obtained from the porous model and predicted by homogenised micropolar and Cauchy models for the loading and geometry demonstrated in Fig. 10. (% error) shows the difference between values resulted from the homogenised model and the detailed porous model.

Distribution	*L*/*W*	Porous	Micropolar	(% error)	Cauchy	(% error)
A	0.55	10.50	11.20	(6.67)	11.50	(9.52)
	1.00	5.04	5.34	(5.95)	5.51	(9.33)
	1.55	3.58	3.76	(5.03)	3.95	(10.34)
	2.00	3.20	3.33	(4.06)	3.55	(10.94)
X	0.55	12.61	13.14	(4.18)	13.53	(7.27)
	1.00	6.98	7.17	(2.65)	7.47	(7.00)
	1.55	5.53	5.56	(0.67)	5.91	(6.88)
	2.00	5.16	5.11	(-0.85)	5.51	(6.80)
V	0.55	6.93	7.12	(2.70)	7.33	(5.77)
	1.00	4.29	4.31	(0.36)	4.47	(4.09)
	1.55	3.63	3.56	(-2.10)	3.75	(3.18)
	2.00	3.47	3.34	(-3.74)	3.56	(2.53)
O	0.55	10.07	10.42	(3.44)	10.58	(5.02)
	1.00	5.58	5.69	(1.94)	5.78	(3.46)
	1.55	4.45	4.46	(0.35)	4.56	(2.51)
	2.00	4.16	4.13	(-0.74)	4.25	(2.16)

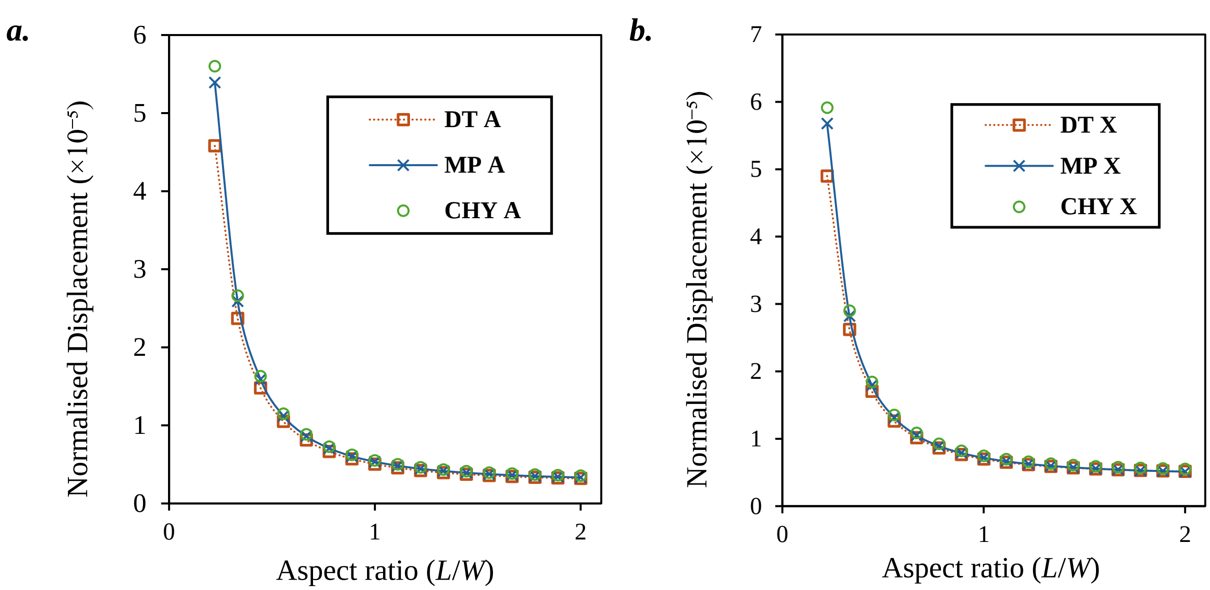

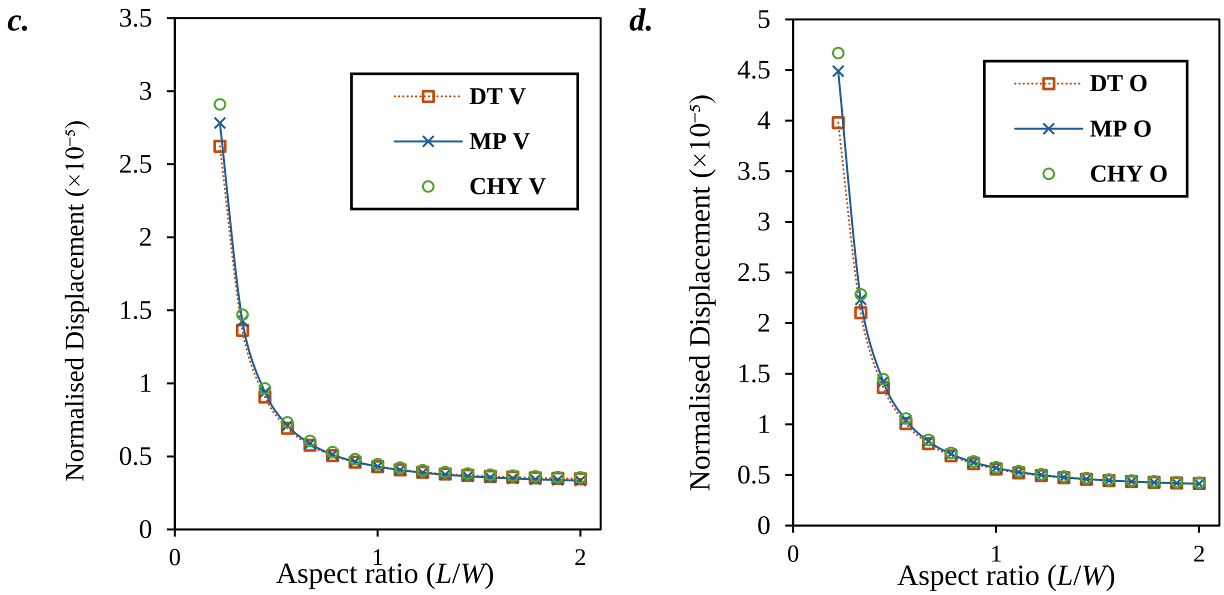

*Fig. 13 Comparison of maximum normalised displacement (normalised displacement at Point A in Fig. 10) in the porous and homogenised models for different aspect ratios and porosity distribution of **a.** Type A, **b.** Type X, **c.** Type V, **d.** Type O*

4.4 The effect of different porosity distributions

To study the effect of different porosity distributions, the maximum deformations of the homogenised models for four types of porous FG structures are compared.

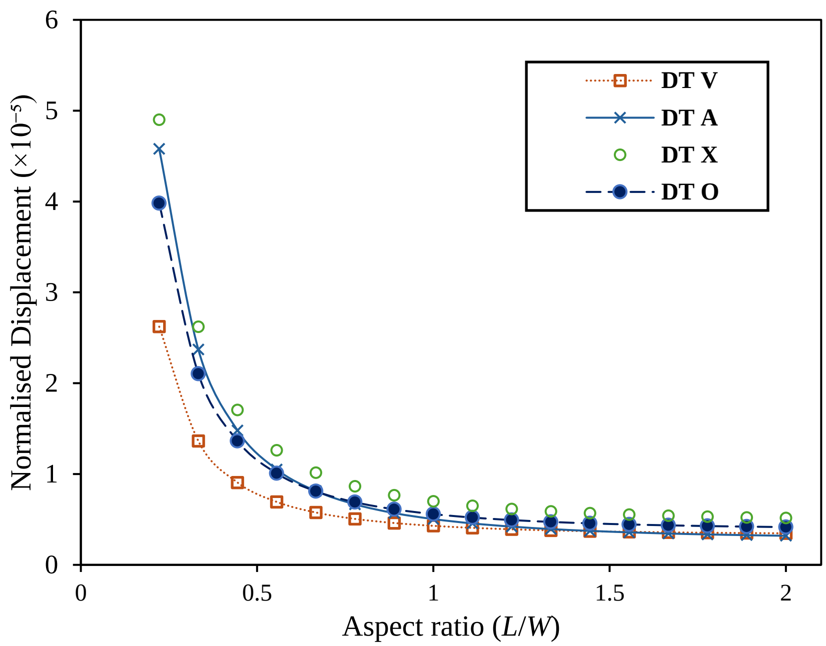

Fig. 14 Comparison of the maximum normalised displacement (normalised displacement at Point A in Fig. 10) of the FG porous plate for porosity distribution Type 'A', Type 'V', Type 'X', and Type 'O' for various aspect ratios.

As can be inferred from Fig. 14 for aspect ratios less than approximately 1.5, it is important to take functional porosity into account when predicting the plate's mechanical response; however, in higher aspect ratios, the overall porosity plays a more important role. This becomes clearer by comparing the maximum displacement for two distribution types A and V reported in Table 3, with the overall same porosity. As shown in the table, the difference between maximum displacement is high for L/W=0.5 and decreases for L/W=1.5 and 2.

Table 3 Comparison of the maximum normalised displacement (normalised displacement at Point A in Fig. 10) for porosity distributions Type 'A' and Type 'V'. The values in the parentheses show the difference between the A and V distributions for each AR.

Distribution	Porosity	Volume Fraction	Max Normalised Displacement					
			L/W=0.5		L/W=1.5		L/W=2.0	
Type A	20.14 %	0.79858	10.50	(52%)	3.58	(1%)	3.20	(7%)
Type V	20.14 %	0.79858	6.93		3.63		3.47	

4.5 Indentation of a Vertical Load

To provide further evaluation of the proposed model, another loading scenario is studied in this section for all the FG patterns. Fig. 15 shows the loading and boundary condition on an FG plate with the O pattern as an example.

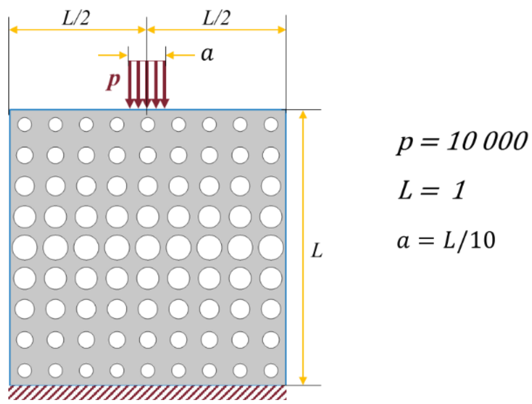

Fig. 15 The geometry, loading, and boundary conditions for the vertical indentation on an FG porous structure with porosity distribution Type O

The maximum normalised displacement observed in the FG porous structures with different patterns and the predicted values by the micropolar and Cauchy continua are compared in Fig. 16. This figure shows that in all the patterns, the prediction of the micropolar theory is closer to the real porous structure compared to the Cauchy predictions.

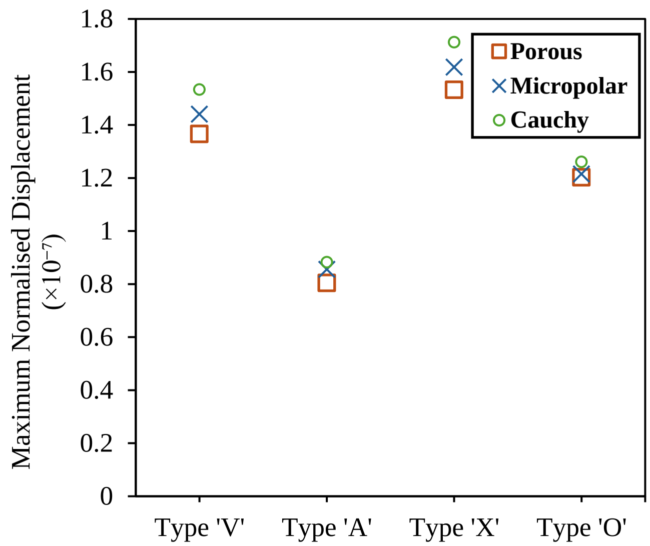

Fig. 16 Comparison of maximum normalised displacement resulted from the vertical indentation in the porous and homogenised models for different porosity distributions of Type A, Type X, Type V, and Type O.

Besides in Fig. 17, the contour of the normalised displacements for the FG porous structure with V pattern and the homogenised micropolar and Cauchy models are compared. As can be seen, the load penetration reflected in the displacement contours is better captured by the micropolar model compared to the Cauchy one.

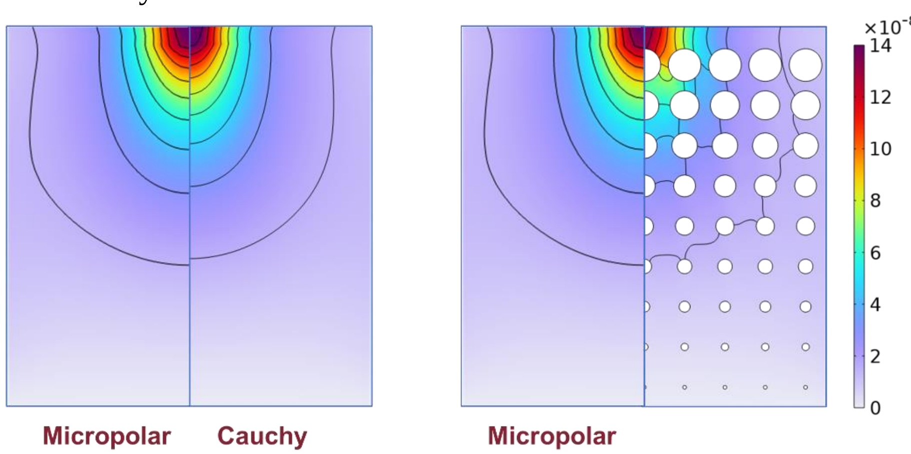

Fig. 17 Comparison of normalised displacement contours of the porous model versus homogenised micropolar and Cauchy models for FG porous structure with porosity distribution Type V

5 Case Study: FG porous design in GBR dentistry meshes

From a mechanical and physiological perspective, it is important that bone scaffolds mimic the mechanical characteristics of the host bone to prevent a phenomenon known as stress shielding. Stress-shielding happens when an over-rigid implant reduces the stress in its adjacent bone. Since loading is necessary to promote bone remodelling, this could prevent bone regeneration and result in bone resorption. Conversely, an extremely flexible implant may cause undue stress on the bone, impairing the consolidation of the bone-implant interphase and ultimately resulting in the death of bone cells [74]. Therefore, based on the developed framework in the current work, the following design is suggested for the GBR mesh made from bioresorbable PLA.

By mimicking the FG natural structure of the bone, an FG structure of type O is suggested, as shown in Fig. 18, so that the central part of the GBR mesh possesses mechanical properties close to cancellous (trabecular) bone while providing a proper occlusivity and the part near fixing areas (the screw's location) as near as possible to cortical (compact) bone to provide required load-bearing capacities.

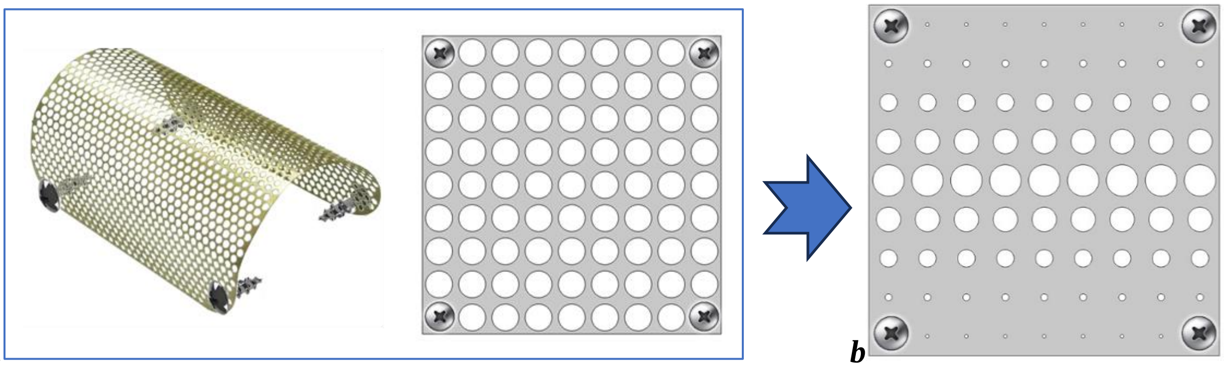

*Fig. 18 **a.** The usual porous GBR meshes implemented with uniform porosity **b.** FG porous structure (Type O) design*

However, the experimental micropolar parameters for mandible cancellous bone are not available in the literature. Also, it should be noted that these parameters can vary depending on different factors such as the patient's age, gender, and health status [75].

An estimate of the mechanical parameters of mandible cancellous bone is reported in Table 2 retrieved from [75], [76], and considering $A_{1111}=\dfrac{E(1-\nu)}{(1+\nu)(1-2\nu)}$ and $A_{1122}=\dfrac{E\nu}{(1+\nu)(1-2\nu)}$ from linear elasticity for isotropic materials [77].

Table 4 Mechanical parameter data available for mandible cancellous bone adapted from [75], [76]

Parameter		Value	Unit
Young's Modulus	E	0.907	GPa
Poisson Ratio	ν	0.3	-
A_{1111}		1.84	GPa
A_{1122}		0.79	GPa

According to the studied configurations in the current work, pore sizes of $0.075W$ can provide mechanical parameters near those of the cancellous bone in Table 4. This is suggested as the pore size in the middle of the GBR mesh.

For the GBR parts around the fixing area, a minimum pore size of $0.01W$ is suggested to allow for enough permeability for the nutrients. Considering that W is around one centimetre for dental GBR meshes, the pore size of $0.01W$ is in favour with the experimental observation of Gutta et al. [55], where they reported that macro-pores of more than 1 mm promote better bone regeneration [60].

However, it should be noted that the micropolar parameters corresponding to the pore size of $0.01L$ in a PLA porous plate are lower than that of the cortical bone. The micropolar parameters of the compact bone retrieved from an experimental report [78], [79], are presented in Table 5. However, this can be remedied by locally reinforcing the base material in these areas; a suggestion is to use nano-reinforcements such as silver nanoparticles. Introducing a nano-reinforcement like silver nanoparticles into PLA [80] will enhance its mechanical properties [81] and endow antimicrobial features to the material, which is of great interest in GBR meshes [82]. For instance, as reported in [81], adding 21.8% weight fraction of silver nanoparticles to PLA will improve the Young's modulus by 2.75 times, and this will roughly increase all the parameters with the same order, thus making the parameters of the porous structure with $0.01L$ close to the ones reported in Table 5. The full investigation of the effect of nano-reinforcement and the design of functionally graded materials (FGM) in conjugation with functionally graded porosities can be the topic of future investigations.

Table 5 Micropolar stiffness matrix components for bone extracted from experimental data [2]

Parameter	Unit	Value
A_{1111}	GPa	12.00 ~ 43.43
A_{1122}	GPa	4.00
A_{1212}	GPa	21.10 ~ 36.77
A_{1221}	GPa	-13.05 ~ 2.67
D_{11}	kN	3.24

6 Conclusions

In the current work, non-classical micropolar and Cauchy continua are proposed to model porous plates with functionally graded distribution of porosities within the plane. A multiscale approach is developed based on the equivalence of strain energy to find the material properties of homogenous continua equivalent to heterogenous FG porous structures. To evaluate the effectiveness of the method, the mechanical response of FG porous plates with diverse porosity distributions, 'V', 'A', 'X', and 'O', and a broad range of aspect ratios is compared to the prediction of the equivalent models. To show the applicability of the developed framework, it is used to design a biomedical prothesis used in dentistry called guided bone regeneration (GBR) mesh.
The main findings are summarised as follows:

- The micropolar theory-based modelling can better predict the displacement distribution of the FG porous structure for all porosity patterns compared to the Cauchy-based modelling. The competence of micropolar to Cauchy theory is more prominent in case of A and X patterns. In all cases, the prediction of micropolar theory becomes closer to the porous structure as the aspect ratio increases.
- For aspect ratios less than approximately 1.5, it is important to take functional porosity into account when predicting the FG plate's mechanical response; however, in higher aspect ratios, the overall porosity plays a more important role.
- As a biomedical application of the proposed modelling, it is used to suggest a GBR mesh that tries to mimic the FG natural structure of the bone. The FG porous configuration is suggested so as the central part possesses mechanical properties close to mandible cancellous (trabecular) bone to provide the proper occlusivity and the part near fixing areas provides higher stiffness.

Acknowledgements

The support of PRIN 2020, project 2020F23HZ7_003 (grant number: J35F22000640001), Ministry of University and Research (MUR) is acknowledged by Nicholas Fantuzzi.
The support of the Italian Ministry of University and Research [No. 1062 of 10/08/2021, the endowment of the PON "Research and Innovation" 2014-2020] is acknowledged by Razie Izadi.

References

[1] C. Xu, M. Li, J. Huang, and S. Gao, “Efficient biscale design of semiregular porous structures with desired deformation behavior,” *Comput Struct*, vol. 182, pp. 284–295, Apr. 2017, doi: 10.1016/j.compstruc.2016.12.006.

[2] A. Rezaei, R. Izadi, and N. Fantuzzi, “Equivalent micropolar model for porous guided bone regeneration mesh: Optimum design for desired mechanical properties,” *Appl Math Model*, vol. 131, pp. 737–763, Jul. 2024, doi: 10.1016/j.apm.2024.04.008.

[3] L. P. Lefebvre, J. Banhart, and D. C. Dunand, “Porous metals and metallic foams: Current status and recent developments,” *Adv Eng Mater*, vol. 10, no. 9, pp. 775–787, Sep. 2008, doi: 10.1002/adem.200800241.

[4] E. Wang, R. Yao, Q. Li, X. Hu, and G. Sun, “Lightweight metallic cellular materials: A systematic review on mechanical characteristics and engineering applications,” *Int J Mech Sci*, p. 108795, Oct. 2023, doi: 10.1016/j.ijmecsci.2023.108795.

[5] M. Bruggi, H. Ismail, J. Lógó, and I. Paoletti, “Lightweight design with displacement constraints using graded porous microstructures,” *Comput Struct*, vol. 272, p. 106873, Nov. 2022, doi: 10.1016/j.compstruc.2022.106873.

[6] M. R. Barati and A. M. Zenkour, “Electro-thermoelastic vibration of plates made of porous functionally graded piezoelectric materials under various boundary conditions,” *JVC/Journal of Vibration and Control*, vol. 24, no. 10, pp. 1910–1926, May 2018, doi: 10.1177/1077546316672788.

[7] N. Shafiei, S. S. Mirjavadi, B. MohaselAfshari, S. Rabby, and M. Kazemi, “Vibration of two-dimensional imperfect functionally graded (2D-FG) porous nano-/micro-beams,” *Comput Methods Appl Mech Eng*, vol. 322, pp. 615–632, Aug. 2017, doi: 10.1016/j.cma.2017.05.007.

[8] F. Yapor Genao, J. Kim, and K. K. Żur, “Nonlinear finite element analysis of temperature-dependent functionally graded porous micro-plates under thermal and mechanical loads,” *Compos Struct*, vol. 256, Jan. 2021, doi: 10.1016/j.compstruct.2020.112931.

[9] S. Li, S. Zheng, and D. Chen, “Porosity-dependent isogeometric analysis of bi-directional functionally graded plates,” *Thin-Walled Structures*, vol. 156, Nov. 2020, doi: 10.1016/j.tws.2020.106999.

[10] A. Behravanrad and M. Jafari, “Thermo-mechanical behavior of 2D functionally graded porous-auxetic metamaterial rotating disk with an auxetic foundation,” *Aerosp Sci Technol*, vol. 145, Feb. 2024, doi: 10.1016/j.ast.2023.108829.

[11] W. Zhang, C. Wang, and Y. Wang, “Thermo-mechanical analysis of porous functionally graded graphene reinforced cylindrical panels using an improved third

order shear deformable model," *Appl Math Model*, vol. 118, pp. 453–473, Jun. 2023, doi: 10.1016/j.apm.2023.01.026.

[12] T. H. Nguyen, T. T. Nguyen, T. T. Tran, and Q. H. Pham, "Research on the mechanical behaviour of functionally graded porous sandwich plates using a new C1 finite element procedure," *Results in Engineering*, vol. 17, Mar. 2023, doi: 10.1016/j.rineng.2022.100817.

[13] W. Gao, Y. Liu, Z. Qin, and F. Chu, "Wave Propagation in Smart Sandwich Plates with Functionally Graded Nanocomposite Porous Core and Piezoelectric Layers in Multi-Physics Environment," *Int J Appl Mech*, vol. 14, no. 07, Aug. 2022, doi: 10.1142/S1758825122500715.

[14] Ş. D. Akbaş, Y. A. Fageehi, A. E. Assie, and M. A. Eltaher, "Dynamic analysis of viscoelastic functionally graded porous thick beams under pulse load," *Eng Comput*, vol. 38, no. 1, pp. 365–377, Feb. 2022, doi: 10.1007/s00366-020-01070-3.

[15] P. M. Ramteke, S. K. Panda, and B. Patel, "Nonlinear eigenfrequency characteristics of multi-directional functionally graded porous panels," *Compos Struct*, vol. 279, p. 114707, Jan. 2022, doi: 10.1016/j.compstruct.2021.114707.

[16] D. Wu, A. Liu, Y. Huang, Y. Huang, Y. Pi, and W. Gao, "Dynamic analysis of functionally graded porous structures through finite element analysis," *Eng Struct*, vol. 165, pp. 287–301, Jun. 2018, doi: 10.1016/j.engstruct.2018.03.023.

[17] D. Chen, J. Yang, and S. Kitipornchai, "Elastic buckling and static bending of shear deformable functionally graded porous beam," *Compos Struct*, vol. 133, pp. 54–61, Dec. 2015, doi: 10.1016/j.compstruct.2015.07.052.

[18] T. J. R. Hughes, J. A. Cottrell, and Y. Bazilevs, "Isogeometric analysis: CAD, finite elements, NURBS, exact geometry and mesh refinement," *Comput Methods Appl Mech Eng*, vol. 194, no. 39–41, pp. 4135–4195, Oct. 2005, doi: 10.1016/j.cma.2004.10.008.

[19] H. Nguyen-Xuan, K. Q. Tran, C. H. Thai, and J. Lee, "Modelling of functionally graded triply periodic minimal surface (FG-TPMS) plates," *Compos Struct*, vol. 315, p. 116981, Jul. 2023, doi: 10.1016/j.compstruct.2023.116981.

[20] K. Q. Tran, T.-D. Hoang, J. Lee, and H. Nguyen-Xuan, "Three novel computational modeling frameworks of 3D-printed graphene platelets reinforced functionally graded triply periodic minimal surface (GPLR-FG-TPMS) plates," *Appl Math Model*, vol. 126, pp. 667–697, Feb. 2024, doi: 10.1016/j.apm.2023.10.043.

[21] N. V. Nguyen, K. Q. Tran, J. Lee, and H. Nguyen-Xuan, "Nonlocal strain gradient-based isogeometric analysis of graphene platelets-reinforced functionally graded triply periodic minimal surface nanoplates," *Appl Math Comput*, vol. 466, p. 128461, Apr. 2024, doi: 10.1016/j.amc.2023.128461.

[22] E. M. P. Cosserat and F. Cosserat, *Théorie des corps déformables*. A. Hermann et fils, 1909.

[23] A. C. Eringen, "Theory of Micropolar Elasticity," in *Microcontinuum Field Theories*, New York, NY: Springer New York, 1999, pp. 101–248. doi: 10.1007/978-1-4612-0555-5_5.

[24] , AC Eringen and , JL Wegner, "Nonlocal Continuum Field Theories," *Appl Mech Rev*, vol. 56, no. 2, pp. B20–B22, Mar. 2003, doi: 10.1115/1.1553434.

[25] W. Nowacki and W. Olszak, *Micropolar Elasticity*, vol. 151. in CISM International Centre for Mechanical Sciences, vol. 151. Vienna: Springer Vienna, 1974. doi: 10.1007/978-3-7091-2920-3.

[26] S. Hassanpour and G. R. Heppler, “Micropolar elasticity theory: a survey of linear isotropic equations, representative notations, and experimental investigations,” *Mathematics and Mechanics of Solids*, vol. 22, no. 2, pp. 224–242, Feb. 2017, doi: 10.1177/1081286515581183.

[27] R. Bijarnia and B. Singh, “Propagation of plane waves in an anisotropic generalized thermoelastic solid with diffusion,” *Journal of Engineering Physics and Thermophysics*, vol. 85, no. 2, pp. 478–486, Mar. 2012, doi: 10.1007/s10891-012-0676-z.

[28] Q. Wu and Q. Gao, “The symplectic approach for analytical solution of micropolar plane stress problem,” *Int J Solids Struct*, vol. 264, Mar. 2023, doi: 10.1016/j.ijsolstr.2022.112095.

[29] L. Leonetti, N. Fantuzzi, P. Trovalusci, and F. Tornabene, “Scale effects in orthotropic composite assemblies as micropolar continua: A comparison between weakand strong-form finite element solutions,” *Materials*, vol. 12, no. 5, 2019, doi: 10.3390/ma12050758.

[30] S. Forest and K. Sab, “Cosserat overall modeling of heterogeneous materials,” *Mech Res Commun*, vol. 25, no. 4, pp. 449–454, Jul. 1998, doi: 10.1016/S0093-6413(98)00059-7.

[31] E. Scarpetta, “On the fundamental solutions in micropolar elasticity with voids,” *Acta Mech*, vol. 82, no. 3–4, pp. 151–158, Sep. 1990, doi: 10.1007/BF01173624.

[32] R. Kumar and T. Kansal, “Fundamental solution in the theory of micropolar thermoelastic diffusion with voids,” *Computational & Applied Mathematics*, vol. 31, no. 1, pp. 169–189, 2012, doi: 10.1590/S1807-03022012000100009.

[33] M. Ciarletta, A. Scalia, and M. Svanadze, “Fundamental Solution in the Theory of Micropolar Thermoelasticity for Materials with Voids,” *Journal of Thermal Stresses*, vol. 30, no. 3, pp. 213–229, Jan. 2007, doi: 10.1080/01495730601130901.

[34] R. S. Lakes, “Experimental microelasticity of two porous solids,” *Int J Solids Struct*, vol. 22, no. 1, pp. 55–63, 1986, doi: 10.1016/0020-7683(86)90103-4.

[35] M. Marin, E. Carrera, and A. E. Abouelregal, “Structural stability study for porous Cosserat media,” *Mechanics of Advanced Materials and Structures*, pp. 1–9, Feb. 2023, doi: 10.1080/15376494.2023.2172239.

[36] M. Benedetti, A. du Plessis, R. O. Ritchie, M. Dallago, S. M. J. Razavi, and F. Berto, “Architected cellular materials: A review on their mechanical properties towards fatigue-tolerant design and fabrication,” Apr. 01, 2021, *Elsevier Ltd*. doi: 10.1016/j.mser.2021.100606.

[37] N. Fantuzzi, P. Trovalusci, and R. Luciano, “MULTISCALE ANALYSIS OF ANISOTROPIC MATERIALS WITH HEXAGONAL MICROSTRUCTURE AS MICROPOLAR CONTINUA,” *Int J Multiscale Comput Eng*, vol. 18, no. 2, pp. 265–284, 2020, doi: 10.1615/IntJMultCompEng.2020032920.

[38] N. Fantuzzi, P. Trovalusci, and S. Dharasura, “Mechanical Behavior of Anisotropic Composite Materials as Micropolar Continua,” *Front Mater*, vol. 6, Apr. 2019, doi: 10.3389/fmats.2019.00059.

[39] M. Yoder, L. Thompson, and J. Summers, "Size effects in lattice structures and a comparison to micropolar elasticity," *Int J Solids Struct*, vol. 143, pp. 245–261, Jun. 2018, doi: 10.1016/j.ijsolstr.2018.03.013.

[40] Y. Maalej, M. I. El Ghezal, and I. Doghri, "Micromechanical approach for the behaviour of open cell foams," *European Journal of Computational Mechanics*, vol. 22, no. 2–4, pp. 198–208, Aug. 2013, doi: 10.1080/17797179.2013.820979.

[41] Z. Rueger and R. S. Lakes, "Experimental Cosserat elasticity in open-cell polymer foam," *Philosophical Magazine*, vol. 96, no. 2, pp. 93–111, Jan. 2016, doi: 10.1080/14786435.2015.1125541.

[42] R. S. Lakes, "Cosserat shape effects in the bending of foams," *Mechanics of Advanced Materials and Structures*, pp. 1–5, Jun. 2022, doi: 10.1080/15376494.2022.2086328.

[43] R. Izadi, M. Tuna, P. Trovalusci, and N. Fantuzzi, "Bending characteristics of carbon nanotubes: Micropolar elasticity models and molecular dynamics simulations," *Mechanics of Advanced Materials and Structures*, vol. 30, no. 1, pp. 189–206, 2021, doi: 10.1080/15376494.2021.2011499.

[44] R. Izadi, M. Tuna, P. Trovalusci, and E. Ghavanloo, "Torsional characteristics of carbon nanotubes: Micropolar elasticity models and molecular dynamics simulation," *Nanomaterials*, vol. 11, no. 2, pp. 1–20, Feb. 2021, doi: 10.3390/nano11020453.

[45] A. P. Roberts and E. J. Garboczi, "Elastic moduli of model random three-dimensional closed-cell cellular solids," *Acta Mater*, vol. 49, no. 2, pp. 189–197, Jan. 2001, doi: 10.1016/S1359-6454(00)00314-1.

[46] H. Wu, J. Yang, and S. Kitipornchai, "Mechanical Analysis of Functionally Graded Porous Structures: A Review," *International Journal of Structural Stability and Dynamics*, vol. 20, no. 13, p. 2041015, Dec. 2020, doi: 10.1142/S0219455420410151.

[47] N. Wattanasakulpong and V. Ungbhakorn, "Linear and nonlinear vibration analysis of elastically restrained ends FGM beams with porosities," *Aerosp Sci Technol*, vol. 32, no. 1, pp. 111–120, Jan. 2014, doi: 10.1016/j.ast.2013.12.002.

[48] D. Chen, K. Gao, J. Yang, and L. Zhang, "Functionally graded porous structures: Analyses, performances, and applications – A Review," Oct. 01, 2023, *Elsevier Ltd*. doi: 10.1016/j.tws.2023.111046.

[49] L. J. Gibson, M. F. Ashby, G. S. Schajer, and C. I. Robertson, "The mechanics of two-dimensional cellular materials," *Proceedings of the Royal Society of London. A. Mathematical and Physical Sciences*, vol. 382, no. 1782, pp. 25–42, Jul. 1982, doi: 10.1098/rspa.1982.0087.

[50] B. Niu and J. Yan, "A new micromechanical approach of micropolar continuum modeling for 2-D periodic cellular material," *Acta Mechanica Sinica/Lixue Xuebao*, vol. 32, no. 3, pp. 456–468, Jun. 2016, doi: 10.1007/s10409-015-0492-8.

[51] S. A. Faghidian, K. K. Żur, J. N. Reddy, and A. J. M. Ferreira, "On the wave dispersion in functionally graded porous Timoshenko-Ehrenfest nanobeams based on the higher-order nonlocal gradient elasticity," *Compos Struct*, vol. 279, Jan. 2022, doi: 10.1016/j.compstruct.2021.114819.

[52] B. Yang, M. Bacciocchi, N. Fantuzzi, R. Luciano, and F. Fabbrocino, "Computational simulation and acoustic analysis of two-dimensional nano-

waveguides considering second strain gradient effects," *Comput Struct*, vol. 296, p. 107299, Jun. 2024, doi: 10.1016/j.compstruc.2024.107299.

[53] Z. Yang *et al.*, "Advances in Barrier Membranes for Guided Bone Regeneration Techniques," *Front Bioeng Biotechnol*, vol. 10, Jun. 2022, doi: 10.3389/fbioe.2022.921576.

[54] H. Guo, D. Xia, Y. Zheng, Y. Zhu, Y. Liu, and Y. Zhou, "A pure zinc membrane with degradability and osteogenesis promotion for guided bone regeneration: In vitro and in vivo studies," *Acta Biomater*, vol. 106, pp. 396–409, Apr. 2020, doi: 10.1016/j.actbio.2020.02.024.

[55] R. Gutta, R. A. Baker, A. A. Bartolucci, and P. J. Louis, "Barrier Membranes Used for Ridge Augmentation: Is There an Optimal Pore Size?," *Journal of Oral and Maxillofacial Surgery*, vol. 67, no. 6, pp. 1218–1225, Jun. 2009, doi: 10.1016/j.joms.2008.11.022.

[56] Y. D. Rakhmatia, Y. Ayukawa, A. Furuhashi, and K. Koyano, "Current barrier membranes: Titanium mesh and other membranes for guided bone regeneration in dental applications," Jan. 2013. doi: 10.1016/j.jpor.2012.12.001.

[57] R. Izadi, M. Tuna, P. Trovalusci, and N. Fantuzzi, "Thermomechanical characteristics of green nanofibers made from polylactic acid: An insight into tensile behavior via molecular dynamics simulation," *Mechanics of Materials*, vol. 181, Jun. 2023, doi: 10.1016/j.mechmat.2023.104640.

[58] R. Izadi, P. Trovalusci, and N. Fantuzzi, "A Study on the Effect of Doping Metallic Nanoparticles on Fracture Properties of Polylactic Acid Nanofibres via Molecular Dynamics Simulation," *Nanomaterials*, vol. 13, no. 6, p. 989, Mar. 2023, doi: 10.3390/nano13060989.

[59] L. Bai, P. Ji, X. Li, H. Gao, L. Li, and C. Wang, "Mechanical Characterization of 3D-Printed Individualized Ti-Mesh (Membrane) for Alveolar Bone Defects.," *J Healthc Eng*, vol. 2019, p. 4231872, 2019, doi: 10.1155/2019/4231872.

[60] I. Elgali, O. Omar, C. Dahlin, and P. Thomsen, "Guided bone regeneration: materials and biological mechanisms revisited," Oct. 01, 2017, *Blackwell Munksgaard*. doi: 10.1111/eos.12364.

[61] I. Goda, M. Assidi, and J. F. Ganghoffer, "A 3D elastic micropolar model of vertebral trabecular bone from lattice homogenization of the bone microstructure," *Biomech Model Mechanobiol*, vol. 13, no. 1, pp. 53–83, Jan. 2014, doi: 10.1007/s10237-013-0486-z.

[62] I. Goda, M. Assidi, S. Belouettar, and J. F. Ganghoffer, "A micropolar anisotropic constitutive model of cancellous bone from discrete homogenization," *J Mech Behav Biomed Mater*, vol. 16, no. 1, pp. 87–108, 2012, doi: 10.1016/j.jmbbm.2012.07.012.

[63] H. C. Park and R. S. Lakes, "Cosserat micromechanics of human bone: Strain redistribution by a hydration sensitive constituent," *J Biomech*, vol. 19, no. 5, pp. 385–397, Jan. 1986, doi: 10.1016/0021-9290(86)90015-1.

[64] J. F. C. Yang and R. S. Lakes, "Experimental study of micropolar and couple stress elasticity in compact bone in bending," *J Biomech*, vol. 15, no. 2, pp. 91–98, Jan. 1982, doi: 10.1016/0021-9290(82)90040-9.

[65] R. Lakes and J. L. Katz, “Bone and Teeth, Properties of,” in *Encyclopedia of Medical Devices and Instrumentation*, Hoboken, NJ, USA: John Wiley & Sons, Inc., 2006. doi: 10.1002/0471732877.emd042.

[66] Z. Rueger and R. S. Lakes, “Experimental Study of Elastic Constants of a Dense Foam with Weak Cosserat Coupling,” *J Elast*, vol. 137, no. 1, pp. 101–115, Oct. 2019, doi: 10.1007/s10659-018-09714-8.

[67] J. F. C. Yang and R. S. Lakes, “Transient Study of Couple Stress Effects in Compact Bone: Torsion,” *J Biomech Eng*, vol. 103, no. 4, pp. 275–279, Nov. 1981, doi: 10.1115/1.3138292.

[68] J. Fatemi, F. Van Keulen, and P. R. Onck, “Generalized Continuum Theories: Application to Stress Analysis in Bone,” 2002.

[69] N. Fantuzzi, P. Trovalusci, and R. Luciano, “Material symmetries in homogenized hexagonal-shaped composites as cosserat continua,” *Symmetry (Basel)*, vol. 12, no. 3, Mar. 2020, doi: 10.3390/sym12030441.

[70] N. Fantuzzi, F. Shi, M. Colatosti, and R. Luciano, “MULTISCALE HOMOGENIZATION AND ANALYSIS OF ANISOTROPIC ASSEMBLIES AS COSSERAT CONTINUA,” *Int J Multiscale Comput Eng*, vol. 20, no. 5, pp. 87–103, 2022, doi: 10.1615/IntJMultCompEng.2022043195.

[71] Y. Xue *et al.*, “Free vibration analysis of porous plates with porosity distributions in the thickness and in-plane directions using isogeometric approach,” *Int J Mech Sci*, vol. 152, pp. 346–362, Mar. 2019, doi: 10.1016/j.ijmecsci.2019.01.004.

[72] R. Izadi, R. Das, N. Fantuzzi, and P. Trovalusci, “Fracture properties of green nano fibrous network with random and aligned fiber distribution: A hierarchical molecular dynamics and peridynamics approach,” *Int J Eng Sci*, vol. 204, p. 104136, Nov. 2024, doi: 10.1016/j.ijengsci.2024.104136.

[73] S. Farah, D. G. Anderson, and R. Langer, “Physical and mechanical properties of PLA, and their functions in widespread applications — A comprehensive review,” Dec. 15, 2016, *Elsevier B.V.* doi: 10.1016/j.addr.2016.06.012.

[74] Y. Hériveaux, S. Le Cann, M. Fraulob, E. Vennat, V.-H. Nguyen, and G. Haïat, “Mechanical micromodeling of stress-shielding at the bone-implant interphase under shear loading,” *Med Biol Eng Comput*, vol. 60, no. 11, pp. 3281–3293, Nov. 2022, doi: 10.1007/s11517-022-02657-2.

[75] C. E. Misch, Z. Qu, and M. W. Bidez, “Mechanical Properties of Trabecular Bone in the Human Mandible: Implications for Dental Implant Treatment Planning and Surgical Placement,” 1999.

[76] É. Lakatos, L. Magyar, and I. Bojtár, “Material properties of the mandibular trabecular bone,” in *28th Danubia - Adria - Symposium on Advances in Experimental Mechanics, DAS 2011*, Scientific Society for Mechanical Engineering, 2011, pp. 29–30. doi: 10.1155/2014/470539.

[77] M. H. Sadd, *Elasticity*. Elsevier, 2009. doi: 10.1016/B978-0-12-374446-3.X0001-6.

[78] V. A. Eremeyev, A. Skrzat, and A. Vinakurava, “Application of the Micropolar Theory to the Strength Analysis of Bioceramic Materials for Bone Reconstruction,” *Strength of Materials*, vol. 48, no. 4, pp. 573–582, Jul. 2016, doi: 10.1007/s11223-016-9800-1.

[79] V. A. Eremeyev, A. Skrzat, and F. Stachowicz, “Linear Micropolar Elasticity Analysis of Stresses in Bones Under Static Loads,” *Strength of Materials*, vol. 49, no. 4, pp. 575–585, Jul. 2017, doi: 10.1007/s11223-017-9901-5.

[80] H. El-Hamshary, M. E. El-Naggar, A. El-Faham, M. A. Abu-Saied, M. K. Ahmed, and M. Al-Sahly, “Preparation and Characterization of Nanofibrous Scaffolds of Ag/Vanadate Hydroxyapatite Encapsulated into Polycaprolactone: Morphology, Mechanical, and In Vitro Cells Adhesion,” *Polymers (Basel)*, vol. 13, no. 8, p. 1327, Apr. 2021, doi: 10.3390/polym13081327.

[81] A. Rezaei, R. Izadi, and N. Fantuzzi, “A Hierarchical Nano to Micro Scale Modelling of 3D Printed Nano-Reinforced Polylactic Acid: Micropolar Modelling and Molecular Dynamics Simulation,” *Nanomaterials*, vol. 14, no. 13, p. 1113, Jun. 2024, doi: 10.3390/nano14131113.

[82] I. X. Yin, J. Zhang, I. S. Zhao, M. L. Mei, Q. Li, and C. H. Chu, “The antibacterial mechanism of silver nanoparticles and its application in dentistry,” 2020, *Dove Medical Press Ltd.* doi: 10.2147/IJN.S246764.